Liquid slug motion and contact lines in an oscillatory capillary tube

Xiaoqiang Bian[1], William W. Schultz[2,1] and Marc Perlin[1,2]

[1]Department of Naval Architecture and Marine Engineering, University of Michigan, Ann Arbor, MI 48109

[2]Department of Mechanical Engineering, University of Michigan, Ann Arbor, MI 48109

Abstract

Non-wetting liquid slug motions in an axially oscillating horizontal circular tube are studied. We investigate the oscillatory dynamic contact lines that constitute an edge boundary condition for liquid interfacial flow with solid boundaries. To induce oscillatory motion of the liquid slug, the tube is oscillated horizontally along its axis where surface tension and inertia are dominant. Based on the observations, an oscillatory contact line model that considers the unsteady effect is proposed. When the slug acceleration is not large, the meniscus is always a spherical cap and the slug motion can be approximated by an ordinary differential equation in time (a zero dimensional simulation).

For sufficiently slow motion, the model approaches Dussan's (1979) unidirectional steady contact line model. For minimal contact line stick, commonly called contact angle hysteresis, the contact line motion versus contact angle polar plot obtained from both experiments and simulation have elliptical trajectories. When the slug coats the tube with a macro-scale liquid layer for larger forcing velocities, the contact line relation is similar to earlier experiments by Ting & Perlin (1995). This relationship follows the standard definition of hysteresis in that the contact angle depends on the time history of

the contact line velocity, whether or not stick occurs. The model predictions agree qualitatively with the experiments. When the tube oscillation is asymmetric directionally (*e.g.* a truncated periodic t^2 function), a net slug displacement relative to the tube is generated. The pumping effect has potential applications for fluid handling in microgravity or the control of small liquid drops in earth based labs.

1. Introduction

The moving contact line problem has attracted much attention due to its applications in wetting, coating, and capillary wave phenomena, to name a few. A non-integrable stress at the contact line occurs if no-slip is assumed and the Newtonian fluid and non-deformable solid assumptions are satisfied simultaneously (Dussan 1976). The difficulty in treating the contact line problem conventionally arises from the failure of continuum fluid mechanics in the immediate vicinity of the contact area. The nature of the problem suggests the use of molecular mechanics (Thompson & Banavar 1989, Koplik, Banavar & Willemsen 1989). However, the difficulty of a molecular dynamics simulation is not only the vast computation power required to simulate real problems, but that a realistic universal model for the micro-scale physics does not yet exist. Consequently consistent results have yet to appear (Bhatt, Newman & Radke 2002).

Two popular choices have been introduced to remove the singularity depending on the specific system. For non-wetting fluids, a no-slip wall condition is usually relaxed in the immediate vicinity of the contact line. This is not only easier to implement, but also consistent with molecular dynamics simulation (Thompson & Robbins 1989, Koplik & Banavar 1995). Slip models allow solutions of the steadily moving contact-angle problem for creeping flow of fluid advancing on a dry solid surface (Huh & Mason 1977, Hocking

& Rivers 1982, Cox 1986, Dussan, Ramé & Garoff 1991). Numerical approaches for the near contact line flow are usually based on a slip boundary condition (Lowndes 1980, Sheng & Zhou 1992).

Precursor films also eliminate the singularity naturally. One can argue that microscopically, there is always a condensed liquid film ahead of a moving contact line especially for small static contact angles. With a lubrication approximation, this approach is particularly useful in treating slow drop spreading or creeping flows (Chang 1994, Schwartz & Eley 1998). In cases where the film is thin (less than 100 *nm* for water films), disjoining pressure should be included (Derjaguin, Churaev & Muller 1987, Mitlin & Petviashvili 1994).

A complete analysis of many contact-line related fluid dynamic problems rely on an appropriate contact line model. For steady, unidirectional creeping flows, analyses (Cox 1986, 1998; Dussan *et al*. 1991) and numerical studies (Somalinga & Bose 2000) show that over an appropriate range of capillary number Ca (defined as $\mu V_r / \sigma$, where μ is the dynamic viscosity, V_r is the contact line velocity relative to the solid, σ is the surface tension), the velocity field and the meniscus slope in a geometry-independent region can serve as material boundary conditions for outer flows with dynamic contact lines. Apparently, a microscopic study of the moving contact-line problem can potentially provide geometry-free boundary conditions for the outer flow. However, the physics in the immediate vicinity of the contact line is either unclear (the validity of the constant surface tension assumption and the Newtonian constitutive relation, exactness of inter-molecular force/disjoining pressure, etc.) or difficult to measure (Decker, Frank, Suo & Garoff 1999). On the other hand, the apparent contact angle and the flow field are readily

accessible by more conventional measurements where classic hydrodynamics is valid. The dynamic contact-line models based on experiments are capable of solving problems beyond the reach of current full scale analyses or numerical simulations. Therefore the apparent contact angle is studied in this paper.

Although they are often encountered in applications such as capillary wave generation and contact line damping (Hocking 1987, Miles 1990), heat transfer (Tilley, Davis & Bankoff 2001), etc, less is known regarding oscillatory contact lines. The unsteady inertia effects are usually not negligible; therefore analyses similar to unidirectional creeping flow are difficult. Contact line models typically relate the contact angle θ (or local interface slope η_x, where η is the interface displacement relative to the static one, x is the coordinate normal to the solid, and the subscript represents partial differentiation) to the contact line velocity V_r. Thus flows with a contact line boundary are well-posed. Young & Davis (1987) were among the first to study oscillatory contact line motion and they simplified Dussan's model (for unidirectional creeping flow, 1979) to figure 1(a). Their analysis considered slow oscillatory contact line motions and was quasi-static. Hocking (1987) applied the same contact line model in studying waves generated by a vertically oscillating plate penetrating the free surface and in studying the capillary gravity standing wave damping problem. He also gave an analytical solution when contact angle hysteresis was neglected as shown in figure 1b. In studying a similar capillary gravity wave problem, Miles (1990) argued that the contact angle can be proportional to contact line velocity, but that there should be a phase lag for oscillatory motions. This model uses a complex quantity for the proportional constant of Hocking (1987) assuming a simple harmonic analysis. It is sketched in figure 1(c).

It should be noted that in formulating the gravity capillary waves generated by a harmonically oscillating plate, both Hocking (1987b) and Miles (1990) assumed that the generated wave is simple harmonic in time. Even the simplest edge condition linearly relating θ (or meniscus slope if it is small, Hocking 1987) and V_r does not produce a wave that is simple harmonic in time near the oscillating contact line (as shown in the Appendix). Hocking's model is consistent until a time-harmonic analysis is assumed. Miles' model, however, implies that the wave is simple time harmonic *apriori*. Thus, although the resulting ellipse-like contact line relation poses a possible model for oscillatory contact lines, the simple modeling by Miles is not viable.

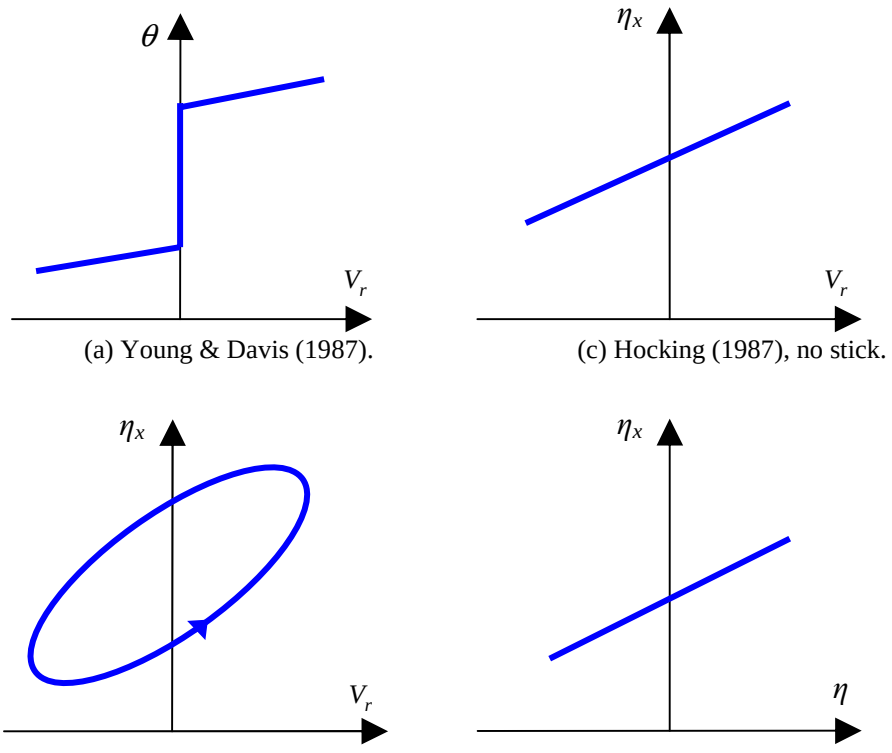

(a) Young & Davis (1987). (c) Hocking (1987), no stick.

(c) Miles (1990), (b) modified by phase lag. (d) Wölk (1997), Bian *et al*. (2003)

Figure 1. Sketches of previous oscillatory contact line models. (a) A direct simplification from Dussan's (1979) unidirectional model. One of the simpler variations is a proportional relation used by Hocking (1987) by neglecting contact angle hysteresis as shown in (b). (c) Miles (1990) used a complex proportional constant for oscillatory motion by explicitly assuming that the contact line velocity and contact line angle are simple harmonic in time. (d) A more qualitative model with linear relation between contact line displacement and interface slope.

Other researchers studied limiting cases applying similar contact line models as in figure 1(a). For small interface perturbations, contact angles can be within the advancing and receding values and remain pinned (Benjamin & Scott 1979, Graham-Eagle 1983, Miles 1987, Bian *et al.* 2003). West's (1911) measurement on a moving mercury column in a capillary tube suggested a contact line model similar to figure 1(a) with zero slope. Kalinitchenko *et al*. (1998) took advantage of the same nonlinearity and generated mean motion of a liquid interface with sinusoidally changing pressure. A more qualitative model describing the linear relation between interface slope and contact line displacement, shown in figure 1(d), has also been used for oscillatory contact line motions (Wölk, Dreyer & Rath 1997, Bian *et al.* 2003). It should be noted that this edge condition is non-dissipative and compatible with the assumption of a time harmonic interface for capillary wave motion.

The accuracy of these oscillatory contact line models, however, has not been properly evaluated. Cocciaro, Faetti & Festa (1993), Ting & Perlin (1995) were the first to measure the oscillatory contact line motion and attempt to specify the boundary conditions. The proposed proportional coefficient λ between the contact angle and the contact line velocity, or the slope in figure 1(a) was measured, but was found to be velocity dependent. A typical oscillatory contact line relation as measured by Ting & Perlin (1995) is shown in figure 2. This relationship looks much different than the previously proposed contact line models. We will show this also agrees with some observations in our experiments.

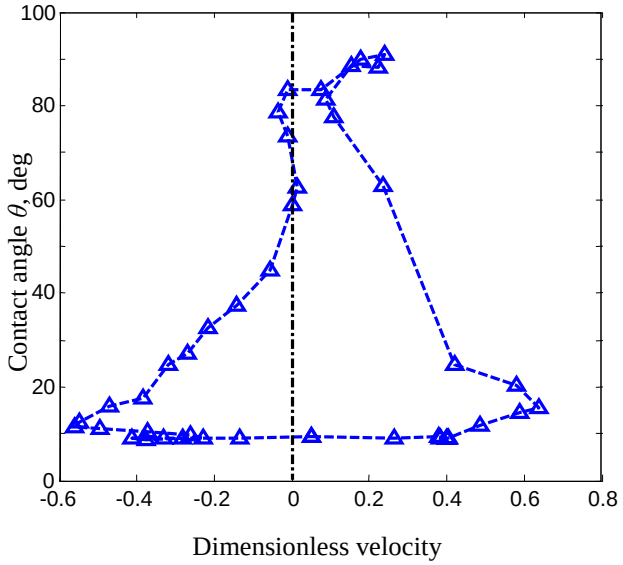

Figure 2. A typical measurement for the oscillatory contact line relation by Ting & Perlin (1995) that resembles a fattened, inverted 'T'. Data are from a glass plate oscillating vertically in a water bath with frequency f = 12 Hz and amplitude a = 3 *mm*.

To facilitate studying contact lines, this investigation considers driving a slug by directional forcing asymmetry. The oscillatory slug flow has applications for modeling multi-phase flow and wave propagation in porous media. For example, Graham & Higdon (2000) demonstrate multiphase flow enhancement in tubes with pressure oscillation or pulsing coupled with a mean pressure gradient. For wetting cases, similar steady problems have been studied experimentally (Taylor 1961), analytically (Bretherton 1961) and numerically (Ruschak 1980, Martinez & Udell, 1989, Giavedoni & Saita 1997). Even for perfectly wetting liquids without contact lines, interfaces in small pores account for a much larger drag than viscosity shear for standard pipe flows (Olbricht 1996). In non-wetting cases, the problem becomes more difficult due to the moving contact line as well as an unsteady, higher Reynolds number flow. An experimental study is thus more practical to investigate the problem.

In this paper, a contact angle–contact line velocity relation is presented and discussed for an immiscible liquid slug in a circular tube with oscillatory forcing. The

apparent contact angle is measured using an indirect method assuming spherical menisci discussed in Section 2. In Section 3, a universal contact line model is proposed based on the observations of oscillatory contact lines. The slug is driven either by tube harmonic oscillation along its axis or by an oscillating pressure gradient. In Section 4, slug net "pumping" motion is introduced by directionally asymmetric (*i.e.* a periodic truncated t^2 motion profile) tube oscillation. The slug motion is simulated by a 0-D approach and the optimal pumping efficiency is sought experimentally and numerically. The paper is summarized in Section 5 and further studies are suggested.

2. Experimental apparatus and procedures

2.1 *Experimental apparatus*

The experimental facilities include one electrodynamic shaker, one feedback controlled servo-motor driven linear positioner, an Argon-ion 6-Watt laser, a Kodak high speed video imager, all setup as shown schematically in figure 3. Two oscillators (shaker and linear positioner) span the system frequency range from slightly less than 1 Hz to more than 20 Hz. Both follow prescribed motions. The prescribed motion profile is either a digital signal to the positioner or an analogue voltage signal to the electrodynamic power module. Two precision ground (to $\pm 0.025\ mm$) borosilicate glass tubes with internal diameters $D = 1.78\ mm$ *and* $3.56\ mm$ and square outer cross-sections, $12.7\ mm \times 12.7\ mm$ may be coupled to the shakers. The square shape is for reduced optical distortion. The liquid slug is formed from HPLC-grade (high-pressure liquid chromatography) water. The water is fluorescein treated to respond to 514.5 *nm* laser light to increase the image contrast, decreasing the static surface tension by approximately 3.5 *dyne/cm* (Ting & Perlin 1995). It is not clear whether the dye alters the

wetting properties of the water slug on borosilicate glass – this is not a problem here as long as it is consistent. To better view the flow a laser sheet is produced by using a cylindrical lens and focusing optics to illuminate the water slug as desired. The imaging system is a Kodak Ektapro CID camera and EM1012 processor with a resolution of 192×239 pixels; and the maximum frame rate is 1000 full frames per second. The total memory is capable of storing 409 complete frames. A sample video image is shown in figure 4.

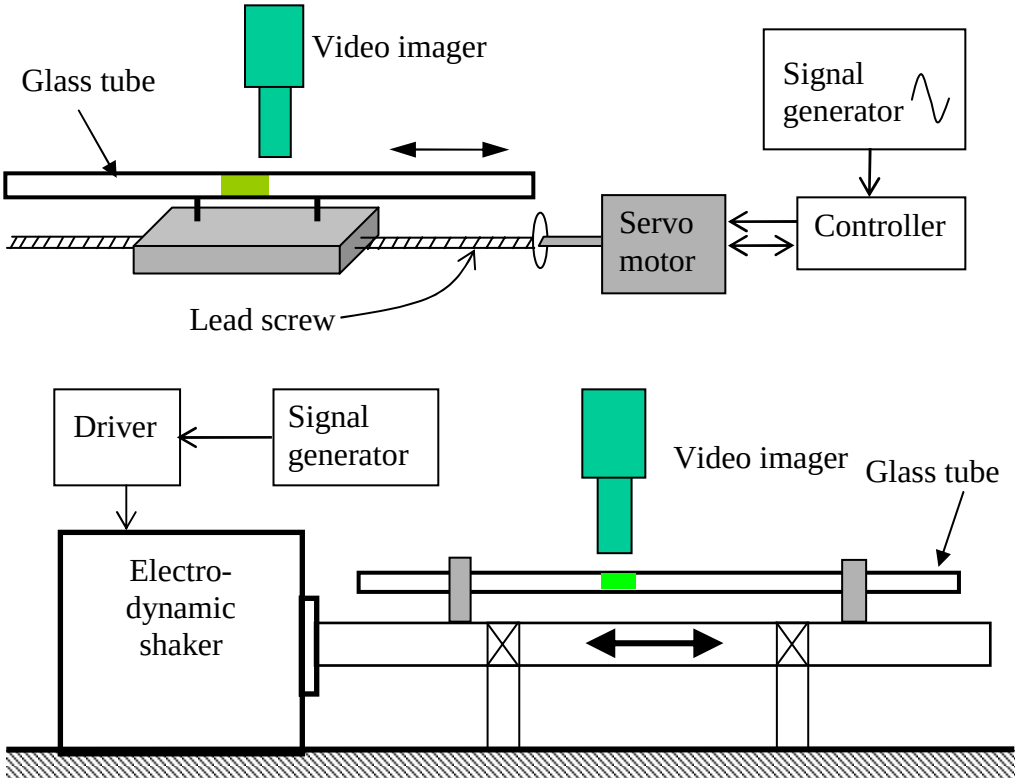

Figure 3. The two experimental setups: The upper schematic shows a lead screw converting motor rotation to linear motion for larger stroke motion and lower frequency (0 to 3 Hz) forcing. The lower schematic shows the electrodynamic shaker used for higher frequencies (2 to 1000 Hz) and smaller stroke amplitude.

Figure 4. A sample image of a liquid slug. A vertical laser sheet is cast through the tube axis from the right upper side. The left meniscus is illuminated by the same laser sheet redirected by a dielectric mirror.

The signal generator is a Dell PC using Windows 2000 with a National Instrument data acquisition board (PCI-6052E) and a Labview (6.0) program. A prescribed periodic t^2 function (see figure 21) horizontally drives the tube displacement to generate mean slug motion. To simplify the analyses and reduce the load on the oscillator, the periodic t^2 function is represented by a filtered 10-term Fourier Cosine expansion. This expansion ensures a smooth second derivative (acceleration). The linear motion system shown schematically in figure 3 is close-loop controlled and the actual motion can be monitored continuously. The electrodynamic shaker is open-loop controlled – the actual input signal is gain and phase compensated to achieve the required motion profile. The actual tube motion signal from a linear displacement sensor is recorded using an additional data acquisition channel and compared with the input signal. We tested sinusoidal and asymmetric tube motion profiles (saw-tooth and periodic t^2 function).

2.2 *Measurement procedures and image corrections*

Preparation of the glass tube and slug of water is as follows: The glass tube is flushed with tap water, then with ethyl alcohol, and last it is flushed with HPLC (high pressure liquid chromatography) water. To test the cleanliness, an HPLC water slug is forced

through the tube by tilting, and if no visible satellite droplets or visible film remains, the cleaning procedure is assumed successful. The procedure is otherwise repeated. The tube is then dried by clean, dehydrated, pressurized air. Next, a fluorescein treated HPLC water slug is inserted to a preset location using a sterile syringe. The slug length is measured relatively easily with a micrometer from contact line to contact line. To increase the uniformity of the contact line and to improve the consistency of the experiments, the tube is pre-wetted by hand tilting and allowing the slug to traverse nearly all the tube length twice. Again, no visible satellite water droplets or film can remain or the tube is deemed contaminated and the cleaning process is repeated. Each experiment records 409 images of 8-bit grey scale resolution, as shown in figure 4 and sketched in figure 6.

The glass tube acts as a concave cylinder lens distorting the recorded images. Figure 5 shows that the diameter of the illuminated slug (left figure with concave meniscus) appears smaller than the actual slug diameter or inner tube diameter due to the refraction by the tube glass. Corrections are therefore required for the images except when using a liquid with the same index of refraction as glass tube (borosilicate glass index $n_g = 1.477$ for 514.5 *nm* laser). Here, water ($n_w = 1.33$) forms the slug (to take the advantage of its large surface tension to minimize gravity effects) so that optical corrections are required. Also, the convex meniscus has increased optical distortion as the light travels through air then glass rather than through water then glass. Using ray tracing, a non-distorted image can be constructed.

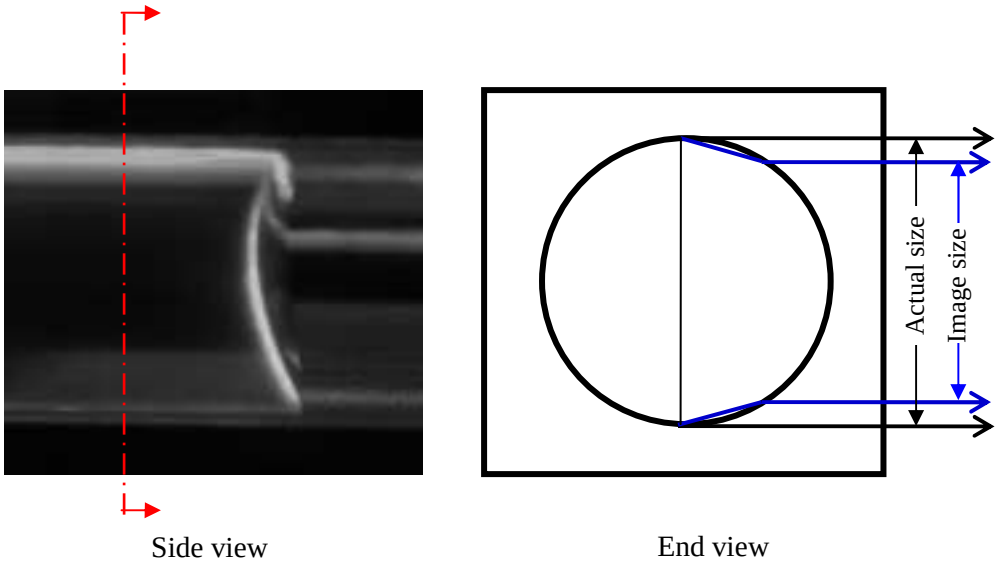

Figure 5. An image of a slug within the circular glass tube with square outer cross section (left). The right sketch shows that the slug appears smaller than it actually is due to light refraction by the tube wall. An undistorted image can be obtained by ray tracing.

The apparent contact angles are measured here by assuming a spherical meniscus. In figure 6, a circle is fitted to match the *distortion corrected* image. The actual meniscus is represented reasonably by a circular arc within our experimental accuracy. Therefore for the subsequent image analysis, only three points, A, B and C in figure 6 are required to determine the upper and lower contact angles, θ_u and θ_l respectively.

Each frame of the recorded video image consists of 192×239 8-bit pixels. The contact line edge is delineated by the maximum grey scale gradient. The tube position is determined from a shadow cast by a marker on the outside of the tube. Using the data structure of the output video, a program analyzes the images, and the positions A, B, C shown in figure 6 are determined as is the synchronized tube position. The contact angle and relative contact line velocity then are obtained as functions of tube position and time.

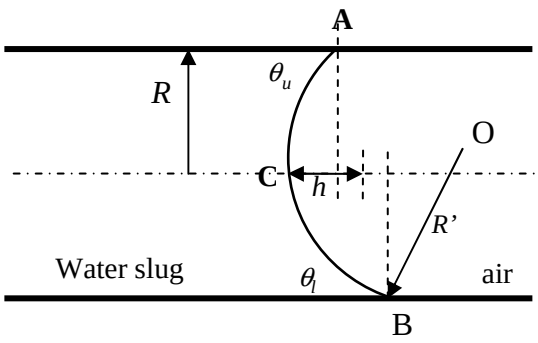

Figure 6. Contact angle measurement with the spherical meniscus assumption. Using positions A, B, and C after image distortion correction, the sphere center O and the sphere radius *R*' can be determined. The upper and lower contact angle θ_u and θ_l are then calculated.

Likewise, to estimate the average apparent contact angle in a simpler way, the average axial distance from C to A and C to B, or *h* in figure 6 are obtained. The average contact angle is $\theta_{ave} = \pi/2 - 2\arctan(h/R)$ according to the spherical meniscus assumption. As can be seen in figure 7, the average contact angle θ_{ave} is approximately the average of the upper and lower contact angles or $(\theta_u + \theta_l)/2$ to within experimental accuracy in our experiments. For convenience, we use θ_{ave} as a reasonable measure for the actual apparent contact angles. Therefore, although the upper and lower contact angles are different due to gravity, its effect that deforms the meniscus is neglected.

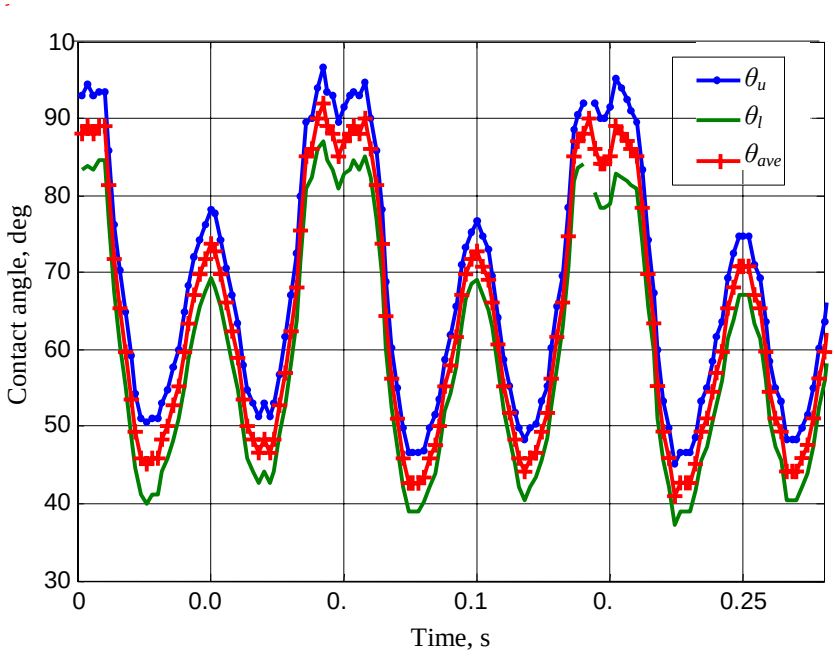

Figure 7. Measured upper contact angle θ_u, lower contact angle θ_l and average contact angle θ_{ave}. Clearly, $\theta_{ave} \approx (\theta_u + \theta_l)/2$.

The macroscopic contact angle measured with a protractor equals the measurement with an indirect method (*i.e.* by measuring the height of the meniscus apex) to within experimental accuracy (Ngan & Dussan 1989). On the other hand, Ramé & Garoff (1996) measured the apparent contact angle θ_{app} with a similar indirect method as that used here and a contact angle extrapolated from the static-like free surface further from the solid, for a cylinder entering a liquid. They found a 2^0 to 3^0 deviation between the two measured contact angles for capillary numbers 0.001 to 0.1. Due to the larger scale and smaller capillary number (Ca < 0.001) in our study, the discrepancy between these two angles is neglected. The primary focus of this study is to investigate the oscillatory contact line motions for a given liquid-solid-air system (such as tube material and surface roughness). The resulting contact line models should be valid for all material

systems having similar inner mechanism, but detailed physical parameters are likely limited only to this system.

3. Oscillatory contact lines – harmonic forcing

Oscillatory contact line motions have been studied by Cocciaro, Faetti & Festa (1993), who measured the contact line on the vertical boundary for a standing wave generated by oscillating a container horizontally. The indicated contact line model was that of figure 1(a) with zero slope. However, according to Jiang *et al*. (2004), the extracted contact angle versus contact-line velocity data based on Cocciaro *et al*. show significant phase delay neglected by the original analysis. Related studies by Ting & Perlin (1995), and Perlin, Schultz & Liu (2004) measured and modeled contact line motions for oscillating vertical plates in water. This research indicates that the basic oscillatory contact line relationship is similar to a fattened, inverted 'T' as in figure 2. These measurements are largely different than previously proposed contact line models based on observations of slow contact line motions. To determine a more consistent model and explain previous observations, contact line motions on horizontal solid surfaces shall be the focus of this study.

3.1. *Measurement of oscillatory contact line motions*

The contact lines of a liquid slug will move relative to the tube when the inertia force generated by the oscillation is sufficiently large to overcome the contact line pinning force. To illustrate the contact angle–contact line velocity relation, measured contact angles are plotted versus contact line velocities for tube motions sinusoidal in time. To generate a sufficiently large dislodging force for the slug with oscillatory forcing, one requires a large value of ωs, where $\omega = 2\pi f$ is the angular forcing frequency and s is

the peak-to-peak tube stroke. That is, a small oscillation stroke with higher frequency or a lower frequency with a larger stroke is required to free the slug. To provide sufficient spatial resolution of the flow requires magnification; however, the resulting field of view of the video camera is consequently unable to accommodate the large strokes required for low frequencies. Therefore for low frequencies, the slug oscillatory motions are driven by air pressure, as shown in figure 8, using a roller (denoted as 'pressure driven') compared to that caused by tube oscillation ('inertia driven'), shown in figure 3.

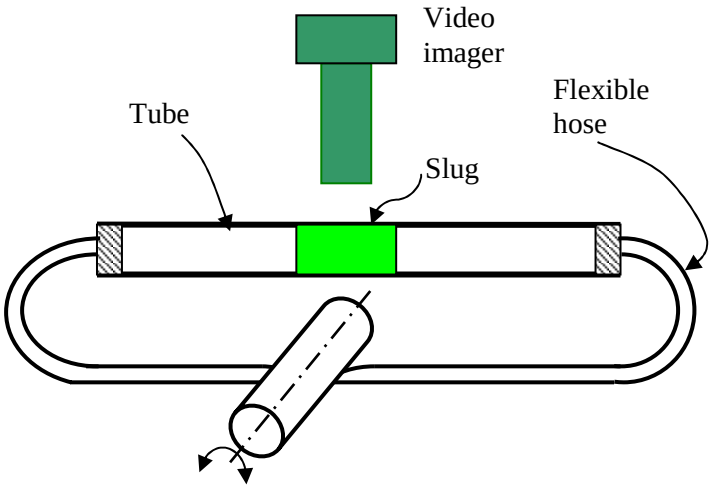

Figure 8. Sketch of the experimental setup for 'pressure driven' contact line motion. The slug is driven by pressure variation caused by sinusoidally rolling a circular cylinder amid the flexible hose length. The liquid slug of $L \times D = 35.5\ mm \times 3.556\ mm$ is placed in the glass tube of length 700 *mm*. The flexible hose is of inner diameter 3 *mm* and total length of 1.6 *m*, the rolling cylinder diameter is 10 *mm*. The same glass tube is used for both sets of experiments.

Polar plots are useful to study the contact angle relation (Ting & Perlin, 1995). Here, contact angles are measured by assuming a spherical end cap (discussed in Section 2), and the contact line velocities are obtained by differentiating the contact line positions relative to the tube. All data are phase-averaged for four cycles to reduce inherent noise. Figure 9 presents the 'inertia driven' oscillatory contact angle versus relative velocity for

a tube oscillating harmonically with frequencies f = 10, 15, and 20 Hz. The tube stroke displacements are s = 1, 1.5, and 2 *mm*. With increasing frequency, the backbones change from a step-function like shape (f = 10 Hz) to an inverted "T' (f = 20 Hz).

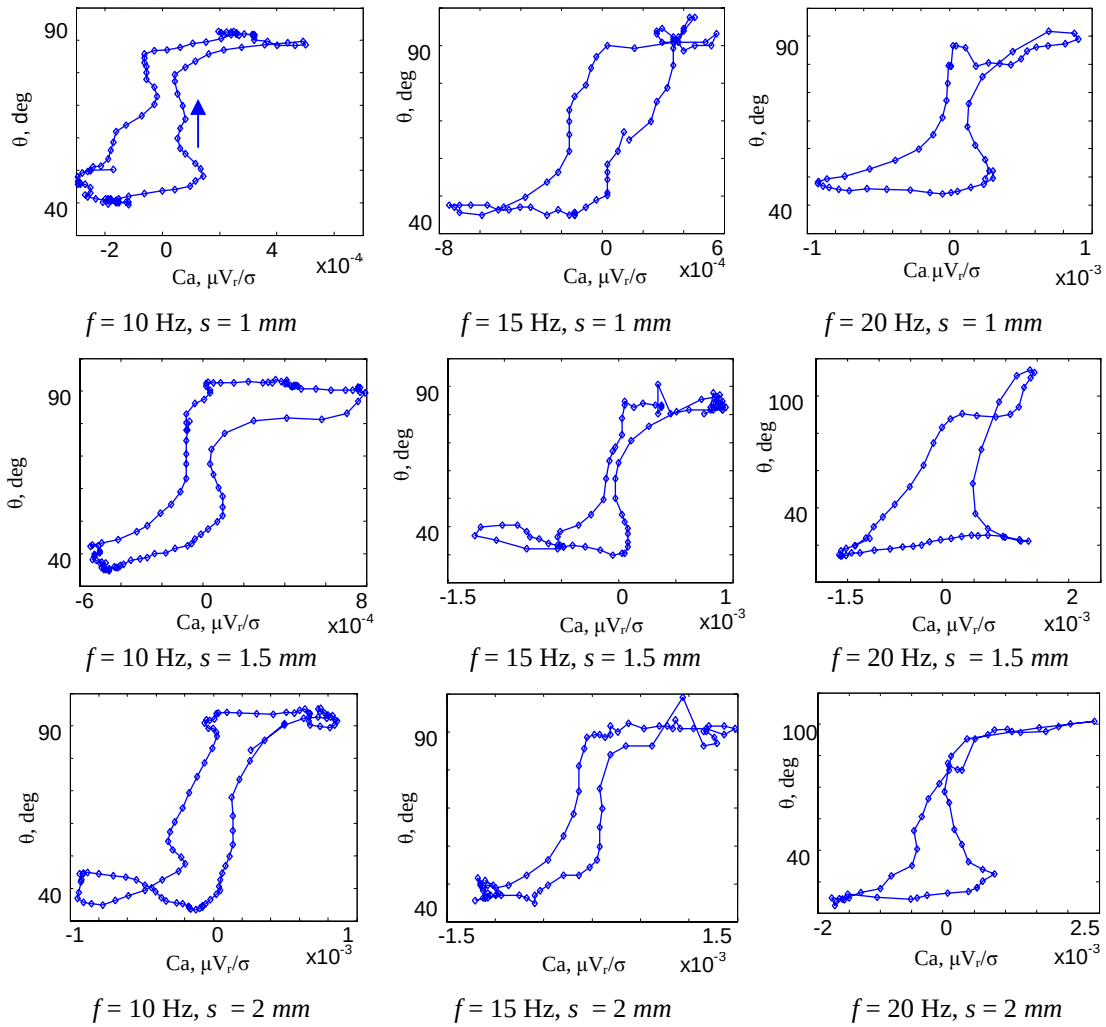

Figure 9. Measured 'inertia driven' contact line polar plots for sinusoidal tube motion. f is the oscillation frequency and s is the peak-to-peak displacement. Slug $L \times D$ = 35.5 *mm* × 3.556 *mm* . The arrow in the first figure gives the general direction of the time increase for all figures.

Due to the high surface tension of water and its ease of contamination, the contact line measurement must be repeated for consistency and careful material preparation is necessary to reduce irregularities. The experiments are completed within 5 minutes and the data are discarded if any thick film or beads appear near the contact lines. Polar plots

still usually contain irregularities and small loop-like structures especially for the larger contact line velocities. The smaller regular loops seem to be caused by an uneven pinning and unpinning mechanism, possibly due in part to surface defects on the tube wall. Another possible reason that may cause smaller repeatable loops is that the slug oscillation may contain higher-modes that violate the spherical cap assumption. Figure 10 shows the polar plots obtained from repeated experiments for tube harmonic motion with f = 10 Hz, s = 2 *mm*. Each figure shows the phase-averaged results of 4 successive cycles. The repeatability of these phase-averaged polar plots is reasonable considering the fast contamination of water. The smaller features are usually not repeatable and are considered a type of experimental noise.

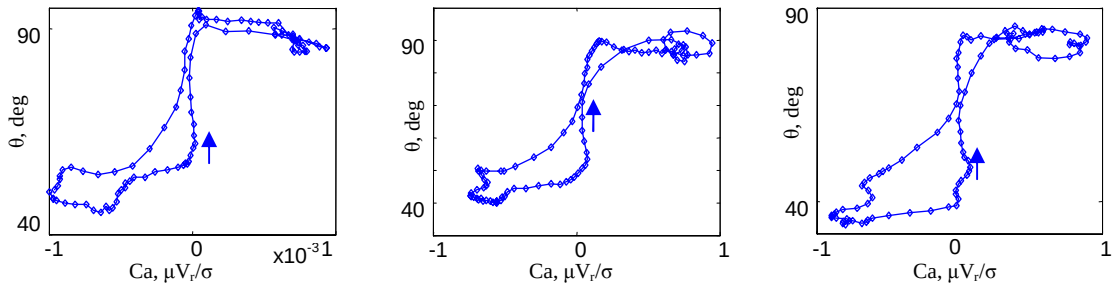

Figure 10. Repeatability of polar plots for inertia driven flow with harmonic forcing f = 10 Hz, s = 2 *mm*. Slug is of L = 35.5 *mm*, D = 3.556 *mm* , and tube length is 700 *mm*.

The pressure driven polar plots for the lower frequencies f = 1 Hz, 5 Hz, and 10 Hz are shown in figure 11. The lateral displacement strokes, s_l, of the rolling cylinder (shown in figure 8) are 5, 10, and 15 *mm*. The 10 Hz results are compared to the polar plots by the inertia driven motion at the same frequency (figure 9), and reasonable agreement is observed. In a sufficiently small tube, the polar plots of both methods would agree more closely.

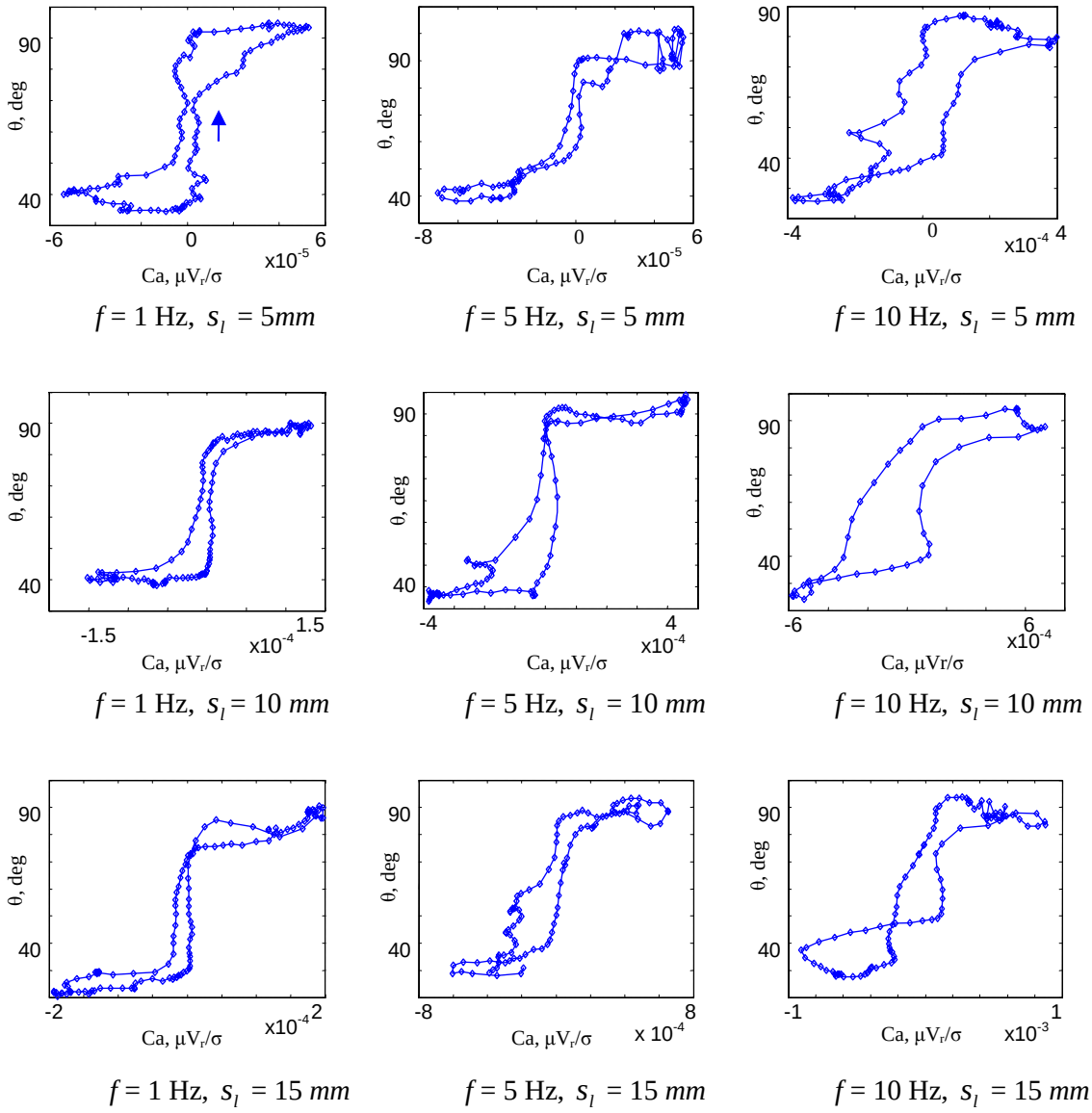

Figure 11. Polar plots by 'pressure driven' flow for frequencies f = 1 Hz, 5 Hz, and 10 Hz and s_l = 5 *mm*, 10 *mm*, and 15 *mm*. The slugs are forced by sinusoidally rolling the cylinder as shown in figure 8. The arrow in the first figure gives the general direction of the time increase for all figures.

Unidirectional advancing and receding contact line motions can be largely different because no unsteady effects and possible macroscopic pre-wetting (for the advancing case) exist. A polar plot for a very slow oscillatory motion presumably approaches that of an unidirectional motion as demonstrated in figure 12 where pressure driven flow is presented for frequency f = 0.2 Hz and lateral rolling cylinder displacement

15 *mm*. As expected, the contact line relation is close to the unidirectional case described by Dussan (1979). The contact angle hysteresis is the typical pure stick for unidirectional motion; the advancing and receding contact angles are approximately 47^0 and 83^0 respectively.

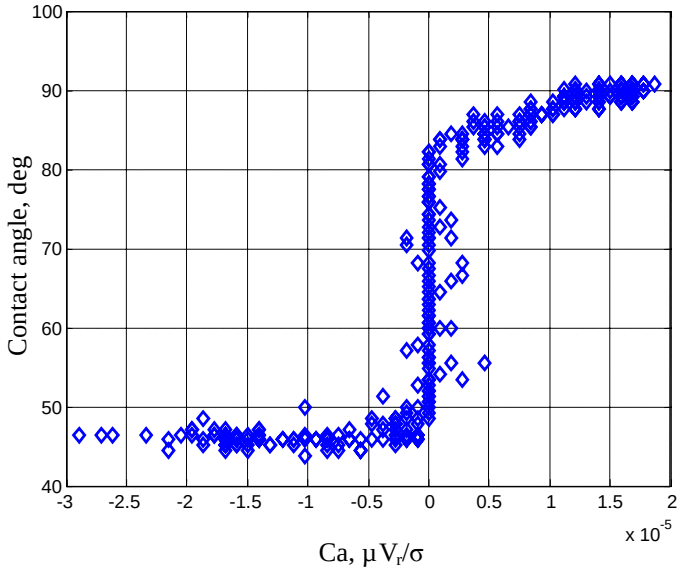

Figure 12. The contact line relation for a slug driven slowly by a harmonically varying pressure. The frequency *f* is 0.2 Hz and the lateral cylinder displacement stroke is 15 *mm*. With very slow oscillatory motion, the results should approach that of a slug moving unidirectionally in a horizontal tube.

Both sets of polar plots for oscillatory contact lines (figures 9 and 11), although exhibiting rich behaviors, are similar in two primary aspects. Firstly, a step-function-like "backbone" resembles the unidirectional moving contact line motion as in figure 1(a) and figure 12. Secondly, the oscillations add a variable phase lag between the contact angle and the contact line velocity. Hence there exists an apparent 'inertial' effect due to unsteady motion. The unsteady effect or 'fatness' of the polar graphs appears to depend more on the frequency than on the contact line velocity (Ca). To illustrate the observed contact line relations, figure 13 shows a sketch with the dotted line representing a generic oscillatory contact line result while the solid line represents a unidirectional, steady

dynamic contact line result. The advancing and receding contact angles are approximately 90^0 and 40^0 respectively for a water slug in a horizontal capillary. The arrow indicates path direction with increasing time. For the unidirectional case, the path direction is immaterial.

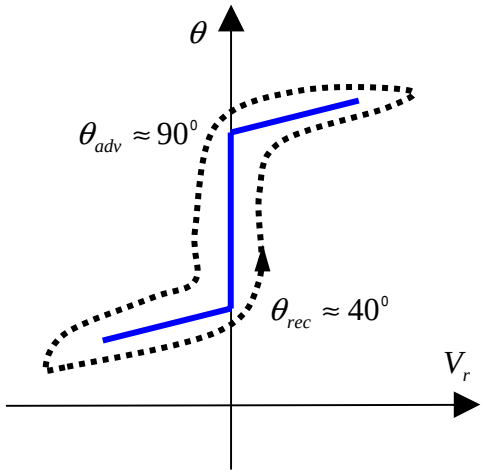

Figure 13. A simplified sketch of the observed polar plots. The oscillatory motion adds a variable phase lag between the contact angle and contact line velocity.

Most polar plots with frequencies from 1 Hz to 20 Hz can be represented by the sketch in figure 13. There are two observations in figure 9 that deviate from the general model of figure 13, especially at 20 Hz. Firstly, the receding contact angles are much less than the receding contact angle, $\theta_{rec} = 40^0$; secondly, the small θ portion of the polar plots overshoots significantly to positive V_r making the plot more closely resemble an inverted 'T' rather than a "fattened" step function. This indicates that advancing contact angles at certain phases approximately equal the receding contact angles. This is similar to previous experimental studies on oscillatory contact lines (Ting & Perlin 1995). It is believed that in these cases, the contact line region is covered with a thick film due to the higher frequencies and/or the larger velocities. Therefore the meniscus is moving partly on a liquid layer. It moves on a less-coated region only when the contact line travels near

the end of its motion. Although lubrication theory fits this case, the unsteady and transient motion of the meniscus, film, and dry solid present a formidable task for analysis. The model depicted in figure 13 should be used for oscillatory contact lines only when the liquid does not significantly coat the solid.

In Ting & Perlin's experiments, almost all the polar plots resemble a fattened inverted 'T', even for small fs as low as $2\ mms^{-1}$ (f = 4 Hz and s = 0.5 mm). Except for possible different wetting properties of their water and glass combination, a very rapid glass surface contamination may have contributed to the thick film deposition. In our experiments, several minutes after a slug is placed in the tube, the water deposits a visible thick film and beads near the contact area, similar to complete wetting – this is evident when the tube wall is illuminated using fluorescein-treated water. Ting & Perlin's experiments are therefore more likely for cases where Newtonian liquid layer deposition occurs, a parameter region beyond most of our experiments.

The contact line velocities are determined by differentiating numerically the contact line displacement with time. Differentiation amplifies noise. Also, due to the uneven contact line motion (contact line velocity exhibits stick-slip motion due to surface roughness and possible contamination), the velocity time series obtained is not smooth. In addition to using local averaging techniques to smooth the velocity curves, here a sine function is used to fit the contact line displacement curve as shown in figure 14. For slow motion (no liquid layer deposit near the contact region), a sine function fits the experimental data reasonably well. However, when the dynamic contact angles are plotted versus the fitted velocities, the polar plots are altered significantly.

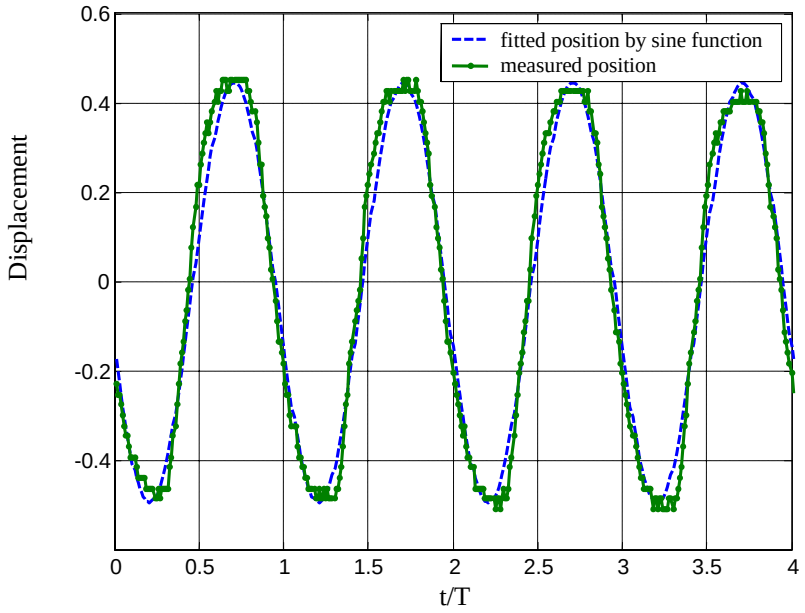

Figure 14. Contact line displacement with sine function fit. The resulting polar plot changes are evident in figure 15.

The polar plots using fitted data as presented in figure 15 are somewhat similar to an ellipse corresponding to some of the results in figures 9 and 11. The fitting process eliminates contact angle hysteresis caused by pinning. Therefore the contact line moves more freely. This fitting forces the process to be time harmonic and hence Miles' model (1990) becomes relevant. The resulting polar plot is close to an ellipse as in figure 1(c) (direct application of Miles' model to the general problem is hampered due to the improper assumption that the contact angle and contact line velocity are time harmonic). Miles also presumed this contact line relation only applies to hydrophilic fluid-solid combinations where capillary hysteresis does not exist. (We assume in this case, however, due to the lubrication effect, that the contact line relation will be more likely similar to a fattened inverted "T" as in the experiments for f = 20 Hz in figure 9 and those of Ting & Perlin in figure 2). In this context, the *elliptical shape* is expected to be the case for oscillatory contact lines relation of those *ideal* systems without static contact

angle hysteresis, i.e. where the unidirectional contact angle – contact line velocity can be described by Hocking's model, figure 1(b).

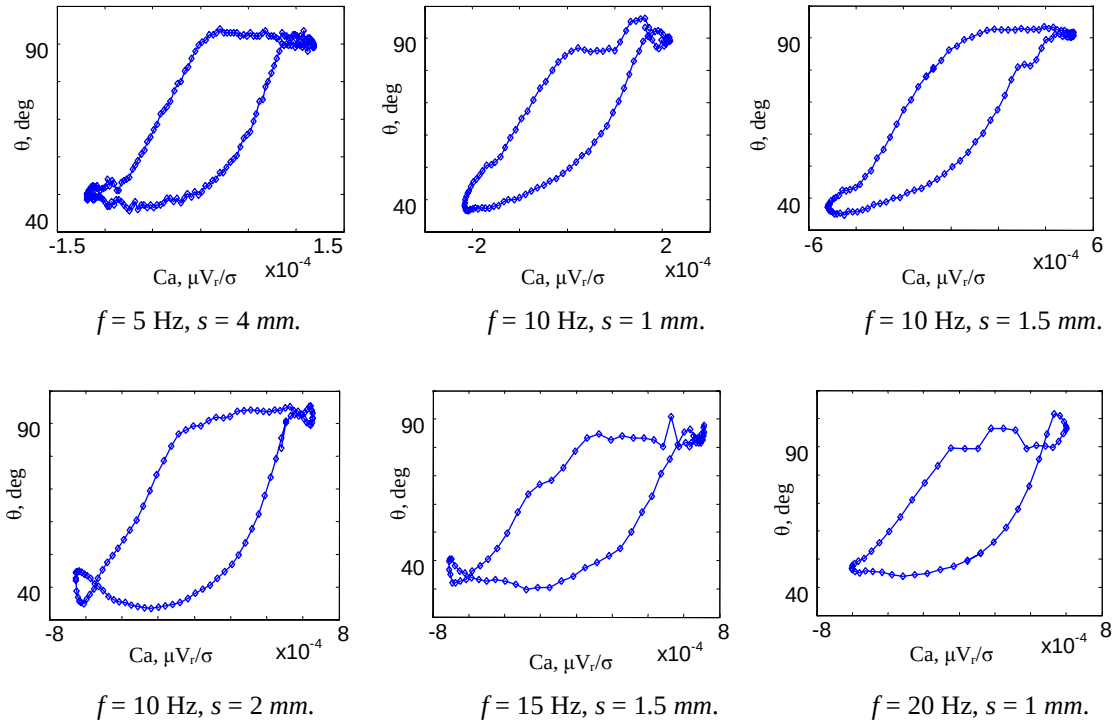

Figure 15. The polar plots where the contact line displacements are fitted by sine functions thus virtually all contact line pinning is removed. The relationship obtained approaches an ellipse. The original data are the same as for those in figures 9 and 11.

3.2. *Oscillatory contact line model and zero dimensional approach*

A model based on experimental observation is constructed following the sketch in figure 13. The "backbone" of the polar graphs is the low-frequency approximation to the unidirectional contact line in figure 12 that is modeled in figure 1(a). The piecewise-linear function is not analytical, so it is replaced with the hyperbolic tangent function (polynomials should work too) to ease the simulation. The backbone may not be a close approximation for slow, unidirectional motion as the pure stick or contact angle hysteresis is eliminated by the model. But for oscillatory contact lines, this is not a

problem as no standard contact angle hysteresis (pure contact line stick with zero contact line velocity) exists. The model takes the following form:

$$\theta_{rel} + \alpha\dot{\theta}_{rel} = \kappa V_r + \gamma \tanh(\beta V_r) + \lambda \dot{V}_r, \qquad (1)$$

where (1) without the terms with time derivatives (dotted terms) is the backbone to describe the slow, unidirectional dynamic contact line motion, and the $\dot{\theta}_{rel}$ and $\dot{V}_r$ terms represent unsteady effects. The parameters κ and β have the dimensions of inverse velocity, λ has the dimensions of inverse acceleration, and α and γ are dimensionless. Here θ_{rel} is the relative contact angle defined as the difference between the actual contact angle θ and the static contact angle θ_s, and is normalized to 1 by $\theta_{rel} = (\theta - \theta_s)/(\theta_{adv} - \theta_s)$.

To apply this contact line model in simulation, a zero dimensional (0-D) approach is used for the inertia driven slug motion. In the 0-D approach, the flow pattern within the slug is neglected and both ends of the slug are assumed spherical. This dramatically simplifies the calculation and still yields reasonable results. The 0-D approach is valid for small Weber and Bond numbers ($We = \rho U^2 R/\sigma$; $Bo = \rho g R^2/\sigma$) and large aspect ratio of the slug L/D >>1.

This 0-D simulation is for slug motion in a horizontal tube that is driven by sinusoidal oscillation of the tube as in the experimental study in figure 9. Now consider the equation of motion of the slug in the tube-fixed coordinate as sketched in figure 16:

$$m\ddot{x}_c + c(V_{r1} + V_{r2})/2 + (\cos\theta_1 - \cos\theta_2)\sigma 2\pi R = -m\,a(t). \qquad (2)$$

Here, m is the mass of the slug, x_c is the center of slug mass in the tube coordinate, c is the viscous friction coefficient for the slug and the enclosed air in the tube as calculated

for steady pipe flow (Poiseuille-flow); V_{r1} and V_{r2} are contact line velocities for the two end caps. The third term on the left-hand side, the stiffness term, is the surface tension force from the contact lines. The shear contribution from the immediate vicinity of the contact line is negligible for smaller Capillary number, Ca (the drag contribution is *0*(Ca) from the shear and is *0*(1) from the surface tension in the inner and intermediate regions, Shikhmurzaev 1997). The right-hand side is the applied force and *a*(*t*) is the prescribed sinusoidal tube acceleration.

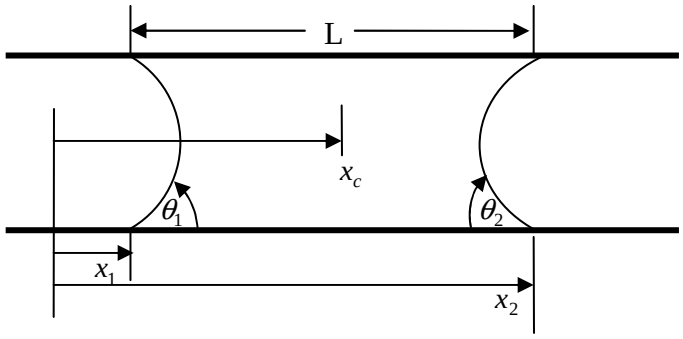

Figure 16. 0-D motion analysis for the liquid slug in the tube-fixed coordinate.

Backward time marching is used to solve for the motion of the center of mass x_c^n, contact angles $\theta_{1,2}^n$, contact line velocities $V_{r1,2}^n$ and slug positions $x_{1,2}^n$ for both end caps at time step *n* under the prescribed tube motion *a*(*t*). The equation of motion in differential form is:

$$m \ddot{x}_c^n + c\,(V_{r1}^n + V_{r2}^n) + (\cos\theta_1^n - \cos\theta_2^n)\,\sigma\, 2\pi R = -m\,a^n(t) \qquad \text{(3a)}$$

$$\dot{x}_c^n = \dot{x}_c^{n-1} + \ddot{x}_c^n \Delta t \;\; ; \;\; x_c^n = x_c^{n-1} + \dot{x}_c^n \Delta t \; . \qquad \text{(3b, c)}$$

The contact line positions x_1 and x_2 are related to the slug center of volume x_c via $\theta_{1,2}$. At any instant, the total volume $\forall$ of the incompressible slug is conserved. The initial

slug length defined from contact line to contact line is L_s, the static contact angle is θ_s. The volume V enclosed by each of the spherical end caps and the plane that includes the contact line is determined by contact angle θ (θ_1 or θ_2):

$$V(\theta) = \frac{\pi R^3}{3} \frac{\cos\theta(2+\sin\theta)}{(1+\sin\theta)^2}. \tag{4}$$

The center of volume for the end cap measured from the plane of the contact line is:

$$h(\theta) = \frac{3-2\sin\theta-\sin^2\theta}{4\cos\theta\ (2+\sin\theta)} R. \tag{5}$$

To maintain the total volume $\forall$ constant, the instantaneous slug length must be determined by the initial slug length L_s and the static contact angle θ_s:

$$\forall = \pi R^2 L_s - 2V(\theta_s) = \pi R^2 L - V(\theta_1) - V(\theta_2),$$

or
$$L(\theta_1, \theta_2) = L_s + \frac{1}{\pi R^2}[V(\theta_1) + V(\theta_2) - 2V(\theta_s)]. \tag{6}$$

The center of mass of the slug is:

$$x_c = x_1 + \frac{\frac{1}{2}\pi R^2 L(\theta_1,\theta_2)^2 - V(\theta_1)h(\theta_1) - V(\theta_2)[L(\theta_1,\theta_2) - h(\theta_2)]}{\forall}, \tag{7}$$

and
$$x_c = x_2 - \frac{\frac{1}{2}\pi R^2 L(\theta_1,\theta_2)^2 - V(\theta_2)h(\theta_2) - V(\theta_1)[L(\theta_1,\theta_2) - h(\theta_1)]}{\forall}, \tag{8}$$

The contact line velocities are determined by:

$$W_{1,2} = (x_{1,2}^n - x_{1,2}^{n-1}) / \Delta t. \tag{9}$$

The contact line velocities and the contact angles are related through the given contact line model (1) in differential form:

$$\theta^{n}_{1,2} + \frac{\alpha}{\Delta t}(\theta^{n}_{1,2} - \theta^{n-1}_{1,2}) = \kappa V^{n}_{r1,2} + \gamma \tanh \beta V^{n}_{r1,2} + \frac{\lambda}{\Delta t}(V^{n}_{r1,2} - V^{n-1}_{r1,2}) \,. \qquad (10)$$

There are seven equations (3a-c, 7-10) for seven unknowns. Using iteration and assuming initial contact line velocities U^{n}_{1} and U^{n}_{2} at time step *n*, the contact angles $\theta^{n}_{1,2}$ can be obtained via contact line model (10), as are the contact line positions $x_{1,2}$. The deduced contact line velocities $W_{1,2}$ by (9) should converge to the initially assumed contact line velocities, $U_{1,2}$. A relaxation technique is used by introducing the weighted average $V^{*}_{1,2}$ of these two contact line velocities

$$V^{*}_{1,2} = aU_{1,2} + (1-a)W_{1,2}, \qquad (11)$$

where *a* is the weight for averaging $U_{1,2}$, and $W_{1,2}$. $V^{*}_{1,2}$ are now substituted back as the initial value $U_{1,2}$ to complete one iteration. A large weight for *a* (~> 0.99) is found necessary for successful convergence of the iteration process (iteration number ≈ 100).

To evaluate the effects of various terms of the model, a simpler version of the contact line model (1) is used:

$$\theta_{rel} + \alpha \dot{\theta}_{rel} = \gamma \tanh \beta V_r \,, \qquad (12)$$

where the advancing and receding contact angles are chosen as 90^{0} and 40^{0} respectively. This model was used for the 0-D simulation for sinusoidal tube motion with *f* = 10 Hz, *s* = 2 *mm*, and L/D = 10. The polar plot obtained and shown in figure 17 is comparable with that in figure 9.

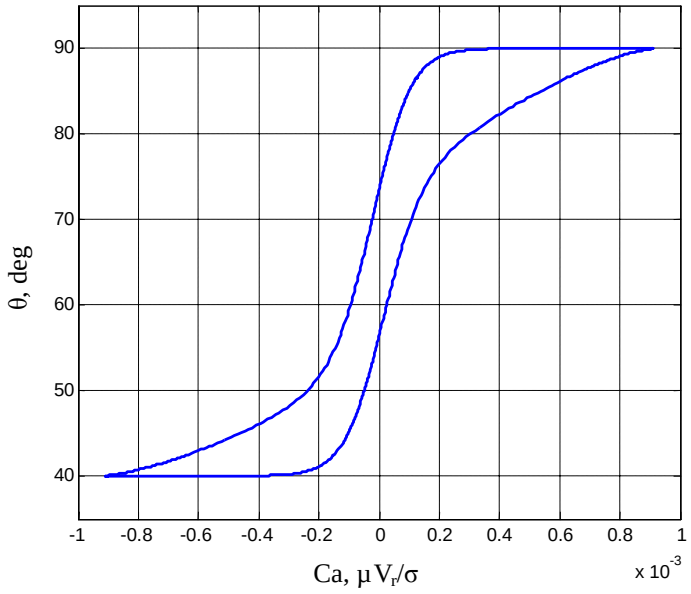

Figure 17. Polar graphs generated by a 0-D simulation for tube harmonic oscillation with f = 10 Hz and s = 2 *mm*. The contact line model is $\theta_{rel} + 0.002\dot{\theta}_{rel} = \tanh 200V_r$. The polar plot is comparable to the experiments presented in figure 9 for f = 10 Hz, s = 2 *mm*. The water slug is L = 35.5 *mm*, D = 3.556*mm*.

The simulated contact line velocity and contact angle variation are compared with the inertia-driven measurements in figure 18 for f =10 Hz, s = 2 *mm*. They compare reasonably well except for the high frequencies present in the experiments. For these particular experimental data, the contact angles have oscillations near 90^0 and 40^0. This motion is caused possibly by a fixed defect on the tube wall as it is not repeatable in our experiments (figure 10). On the other hand, smaller inhomegeneities are usually present that cause smaller irregular contact line motions. Lastly, higher mode oscillations may be present in the experiments.

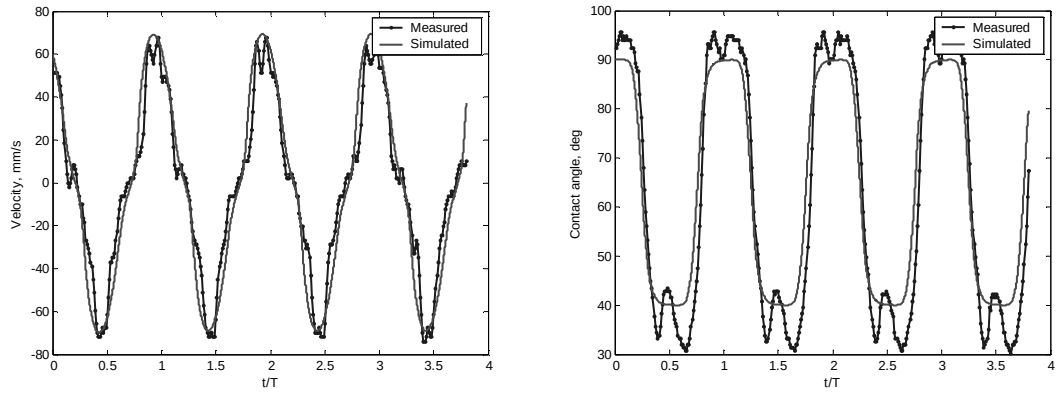

Figure 18. Left: measured and simulated contact line velocities; right: measured and simulated contact angles. Tube harmonic oscillation with f = 10 Hz and s = 2 *mm*. Water slug is L = 35.5 *mm*, D = 3.556 *mm*.

The contact line model (1) can be "fine tuned" to include other observed features. The basic idea is to add the unsteady effect by introducing terms that have time derivatives. The $\dot{V}_r$ term naturally adds more oscillatory effects to the region where velocity changes faster as shown in figure 19 (backbone is fattened on both ends). The coefficients of these additional terms can be variables; for most analyses, simpler models should be sufficient. The parameter-fitting of the model requires more quantitative measurements. The backbone can also be modified. Using a linear function (figure 1b), or Hocking's model as the backbone and adding a simple acceleration term gives a contact line model similar to an ellipse (figure 20). This model does not have the restrictions posed by Miles (1990) that motions are simple time harmonic.

It should be noted that there are cases where no solutions exist for the set of equations (3a-c, 7-10). For instance, the contact-line relation $\theta_{rel} = \gamma \tanh \beta V_r + \lambda \dot{V}_r$ (when λ is negative) failed when the θ – V_r curve has a negative local slope for larger V_r and a positive $\dot{V}_r$. This indicates that a contact-line

relation should be formulated according to experiments and should not be extrapolated outside its range of validity.

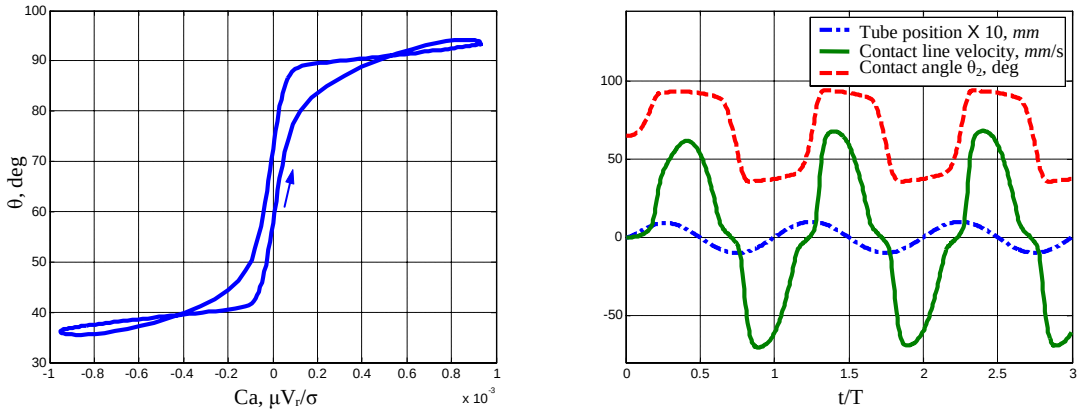

Figure 19. The polar graph (left) and the contact angle variation / contact line velocity (right) predicted by the contact line model $\theta_{rel} + 0.002\dot{\theta}_{rel} = 2V_r + \tanh 200V_r + 0.015\dot{V}_r$ with harmonic forcing. Compared with figure 17, the $\dot{V}_r$ term adds more oscillatory effect where velocity changes faster (on both ends of the backbone curve).

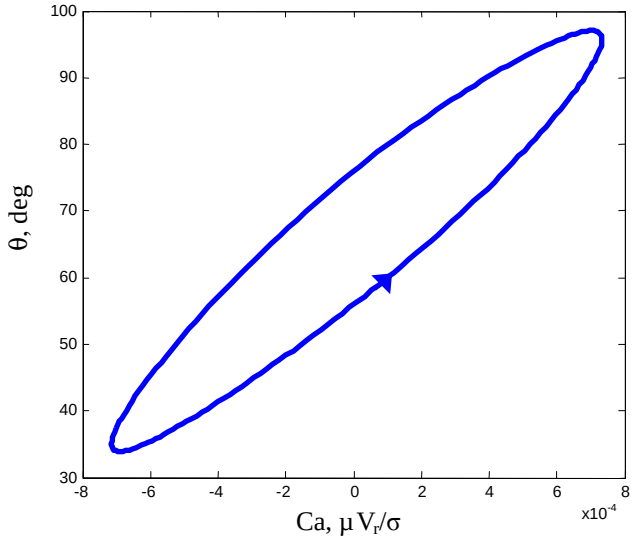

Figure 20. A non-hysteresis backbone (figure 1b) with added unsteady effect: $\theta = \kappa V_r + \lambda\dot{V}_r$. This polar plot generated for harmonic forcing is close to an ellipse.

4. Oscillatory contact lines – asymmetric forcing and liquid pumping

Contact line motions under asymmetric forcing are studied in this section. As discussed in Section 1, the contact angle variation and contact line velocity is not time

harmonic even for simple harmonic tube forcing. The directionally biased contact line motions are expected to provide extra information on oscillatory contact lines as they are more complicated. At the same time, the liquid slug net motion generation provides a possible fluid handling mechanism in microgravity, and is interesting in its own right.

4.1. *Generating net motion by asymmetric oscillation*

Net motion of a slug relative to the tube is driven by a truncated, periodic t^2 horizontal tube motion (figure 21). The t^2 function is chosen because it produces a large acceleration in one direction with shorter duration and a much smaller acceleration in the other direction with longer duration (ratios are a function of the truncation degree). The biased acceleration causes a net motion of the slug relative to the tube. Figure 21 shows a typical mean motion generated by a truncated periodic t^2 motion where the slug moves from one end of the tube to the other end under tube oscillation. The slug relative motion becomes time-periodic after about five initial cycles for the case shown in figure 21. We define the 'pumping efficiency' as the cyclic net displacement of the slug (relative to the tube) Δz divided by the tube peak-to-peak stroke, s. The motion presented in figure 21 has a pumping efficiency of 40%.

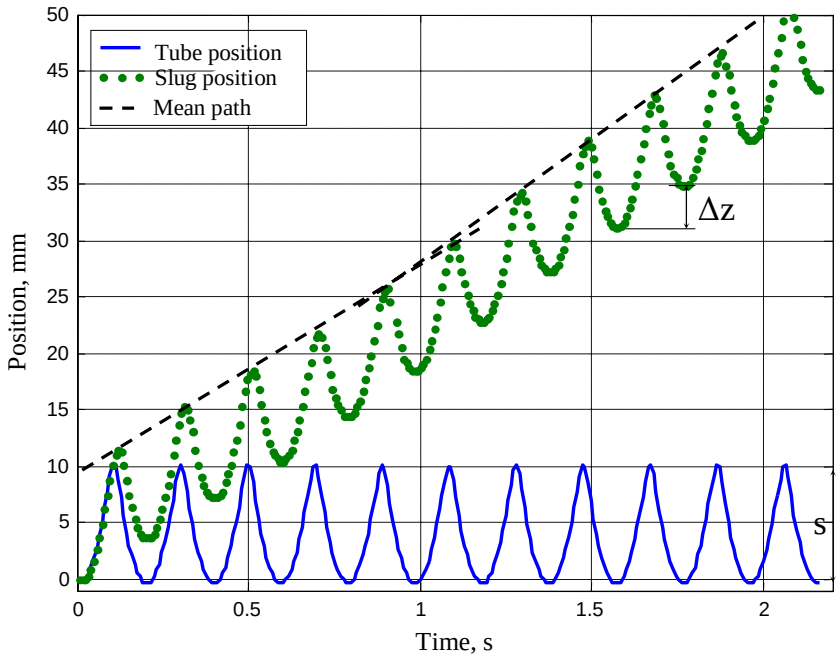

Figure 21. Net motion generated by a periodic t^2 tube motion. The slug mean speed becomes steady after about five cycles. The pumping efficiency for this example is about 40%. D = 3.556 *mm*, L = 10 *mm*.

Figure 22 graphs the measured contact angle θ_{ave} (as described in Section 2 where gravity effects are compensated by averaging upper and lower contact angles) versus the contact line velocity measured for the meniscus on the advancing side of the moving slug. For optimal pumping, the advancing meniscus will experience mostly an advancing contact line, while the other meniscus will experience mostly a receding contact line. The mechanisms for advancing and receding contact lines are apparently different and they were treated as such in steadily moving, long bubble problems by Bretherton (1961). Strictly, the latter case has transition or contact areas rather than true contact lines. For the oscillatory contact line problem however, a simple model is desirable that includes the wetting and de-wetting process in one equation.

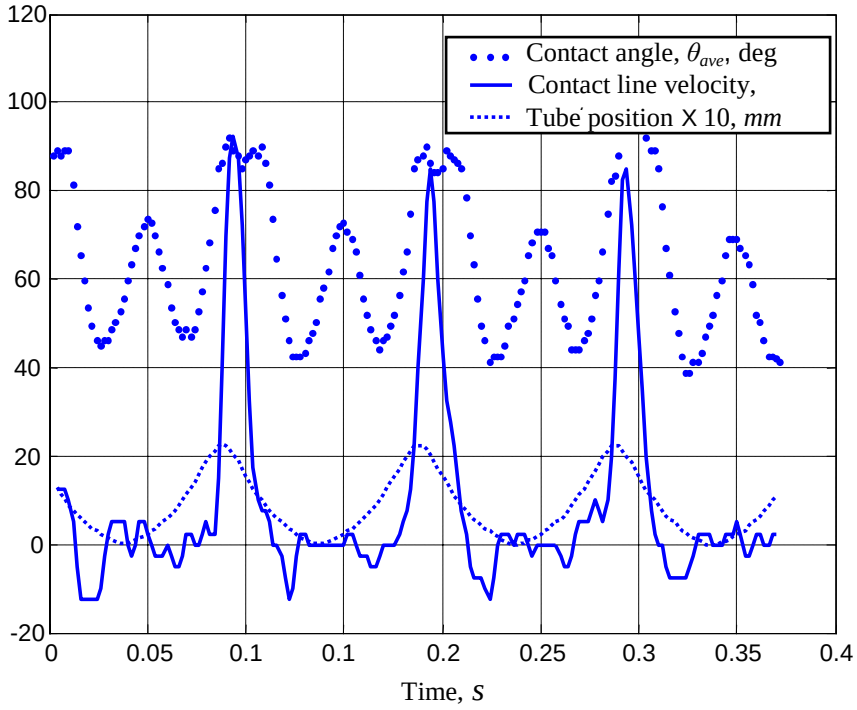

Figure 22. Measured contact angle and relative contact line velocity for the meniscus on the forward side of the advancing slug with D = 3.556 *mm*, L = 10 *mm*. 10-term t^2 tube motion with frequency f = 10 Hz, stroke s = 2.2 *mm.*

Similar to the sinusoidal forcing cases in Section 3, the contact angle versus contact line velocity relationship can be plotted from the measurement in figure 22 for front or rear end caps. The polar plots are generally motion dependent, thus the same contact line relationship will usually result in different polar plot shapes for different forcing. Harmonic motion usually produces an antisymmetric polar plot about the static contact angle. Presented in figure 23 is the polar plot for the front end cap of the slug under periodic t^2 tube motion. The polar plot is asymmetric as the advancing contact line velocity is much larger than the receding velocity, and that generates net slug motion. Apparently, the polar plot in figure 23 can be similarly described as was that of harmonic forcing in figures 9 and 14. The repeatable smaller loop inside the lower part of the graph is a lowest natural mode of the meniscus with a smaller amplitude. Its frequency is about

24 Hz (due to small but evident partial slip in figure 23, it is probably lowered from 28.3 Hz for the complete pinned contact line condition, Bian *et al*. 2003). As shown in Section 4.2, these observations can also be predicted by the contact line model (1).

The contact line polar graphs as measured for the menisci are different on the front end cap (figure 23) and the rear end cap (figure 24) of the slug since one meniscus mostly wets the tube and the other meniscus mostly de-wets the tube. It is also noted that in the polar plots, the contact line velocity is always defined positive for wetting and negative for de-wetting. Thus the larger negative velocity for the rear meniscus in figure 24 is actually in the direction of slug net motion.

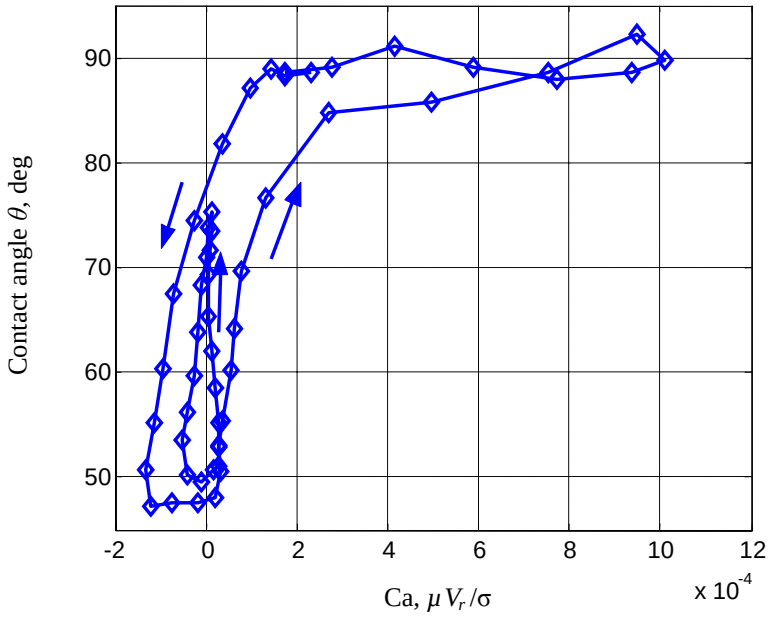

Figure 23. Contact line relation for the meniscus on the front side of the slug moved by periodic t^2 oscillatory tube motion. The figure is phase averaged for eight cycles. These data are for 10-term periodic t^2 tube frequency f = 10 Hz, peak-to-peak tube stroke s = 2.2 *mm*, tube D = 3.556 *mm*, slug L = 10 *mm*.

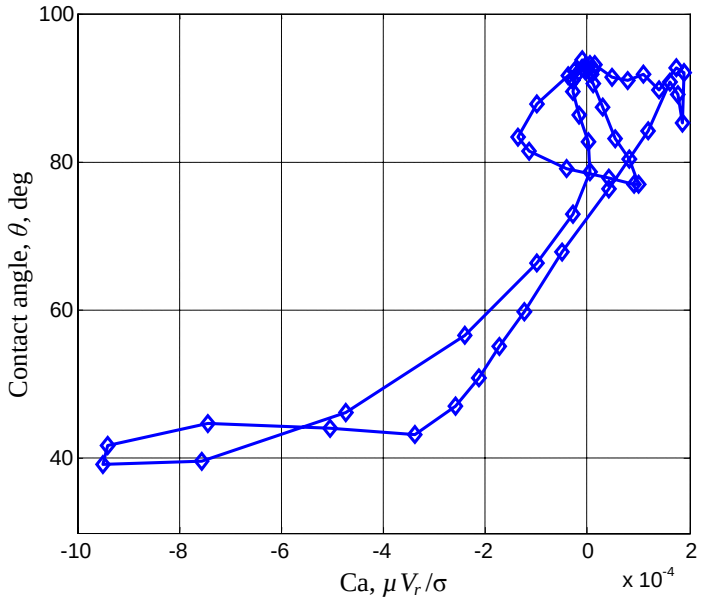

Figure 24. Contact line relation for the meniscus on the rear side of the slug moved by periodic t^2 oscillatory tube motion. The curve exhibits different behavior than that of the front meniscus due to the different nature of the two motions – much different surface wetting conditions of the tube. Tube motion is the same as that for generating figure 23.

The contact line relation with harmonic forcing as shown in figures 9 and 11 is roughly axisymmetric with respect to static contact angle due to the almost symmetric contact line motion. However, this is not the case for asymmetric forcing as figure 23 in conjunction with figure 24 does not generate an approximately axisymmetric function about the static contact angle. Due to the slug net motion and a relatively small field of video image view under large magnification, we have no simple method to record the two menisci simultaneously. Therefore separate videos are recorded for the two menisci, then tube motions are used as a reference to synchronize the data. The velocities and contact angles for both end caps are graphed in figure 25. The contact angles and contact line velocities of the two end caps are approximately in phase. The velocity for the front end cap is larger than the rear end cap, presumably caused by one being mostly an advancing

contact line and the other a receding one. The receding meniscus can be more sensitive to pinning that would also lower the maximum speed.

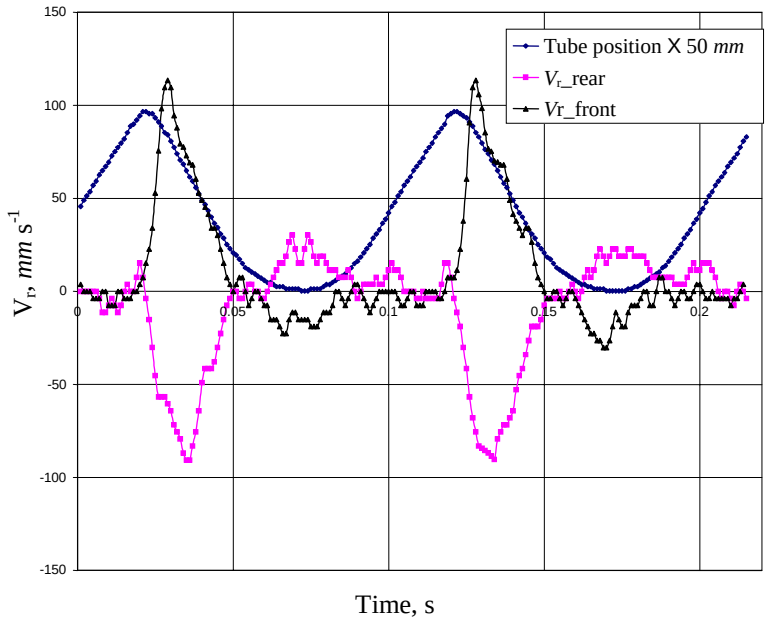

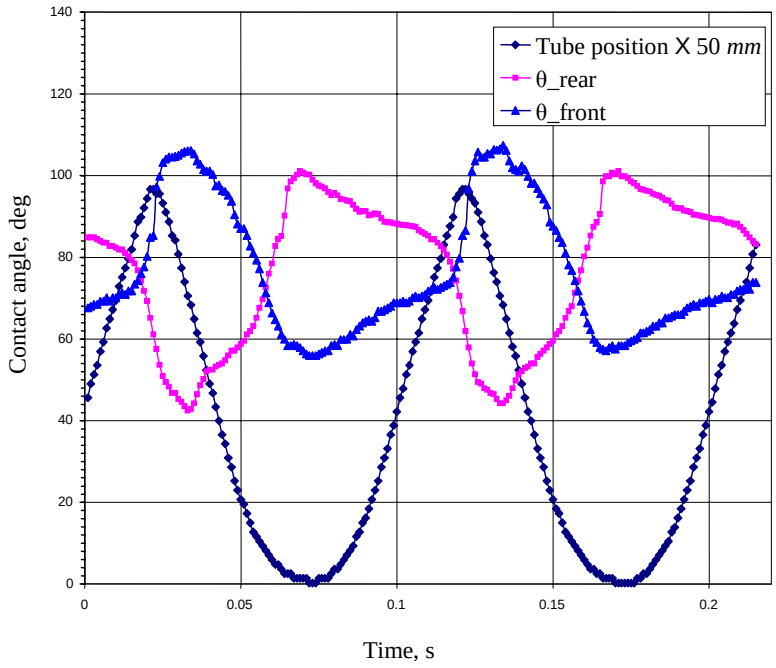

Figure 25. The contact angles and contact line velocities are almost symmetric for the two end caps; however, the maximum contact line velocity for the front end cap is larger. Truncated periodic t^2 tube motion with f = 10 Hz, s = 2 *mm*; water slug D = 3.556 *mm*, L = 20 *mm*.

For axisymmetric oscillation, the optimal parameters are of practical interest. To experimentally determine the maximum pumping efficiency for a given slug, a contour plot for efficiency as a function of drive frequency and stroke is presented in figure 26. The drive frequency is nondimensionalized by the lowest natural slosh frequency of the slug with pinned contact line (see Bian *et al*. 2003). The maximum measured pumping efficiency is about 0.69 for this slug. The region for optimal pumping obtained is roughly at small abscissa, middle ordinate of the contour graph. The optimal frequencies are expected to relate to the natural frequencies of the first slosh mode. The basic idea is to generate resonant slug motion through resonant end cap forcing – this argument is possibly flawed for a very long slug where slip accounts for most of a cycle period. The experiments indicate that the maximum pumping occurs at less than half the frequency of the first slosh mode. We have no explanation for this.

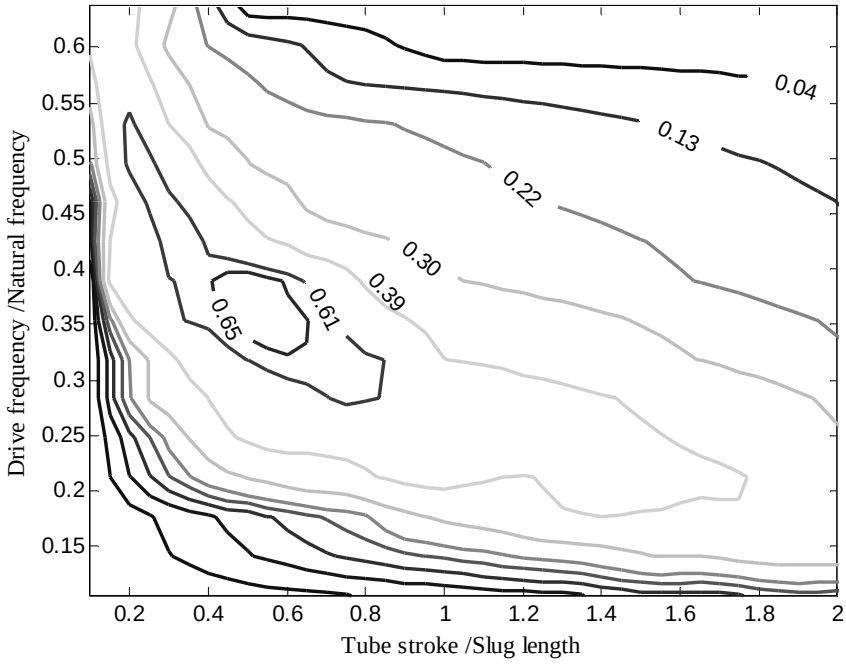

Figure 26. Measured pumping efficiency presented for different drive frequency – stroke combinations. The slug is HPLC water with $D = 3.556\ mm,\ L = 10\ mm;$ the tube is driven by periodic t^2 motion

represented by a filtered 10-term Fourier expansion. The lowest natural slosh frequency of the slug for $\theta_s = 65^0$ with pinned contact line is 28.3 Hz according to the 2-D potential solution (Bian *et al*. 2003).

Other asymmetric tube motions have been tested to achieve pumping, however the periodic t^2 function has so far been the most effective. For instance, the saw tooth function (very slow constant velocity in one direction and maximum system velocity in the other) has been implemented to achieve pumping (Agarwal *et al*. 2001). However, net motion was generated only at very low frequencies (< 0.22 Hz). It is believed that this is due to two identical maximum accelerations per cycle in opposite directions rather than one as for the t^2 case. The maximum force is prescribed necessarily much larger than the pinning force of the contact lines. Therefore the saw tooth function could not fully take advantage of the contact angle hysteresis to retain the slug from moving backward. Consequently at higher frequency the slug moves back and forth relative to the tube rather than moving in one direction. The pumping effect that is achieved at very low frequency is mostly due to the liquid friction, and it is much less effective than contact line drag.

4.2. *Zero dimensional simulation of the slug mean motion*

With a prescribed contact line model, the slug motion can be simulated by the 0-D approach introduced in Section 3. To simulate the net motion, the same truncated periodic t^2 forcing in the experiments is used together with a reduced contact line model:

$$\theta_{rel} + \alpha\dot{\theta}_{rel} = \gamma \tanh \beta V_r , \qquad (13)$$

based on a hyperbolic tangent backbone and added unsteady effects. The polar graph obtained is presented in figure 27 for parameters $\alpha = 0.002;\ \gamma = 1;\ \beta = 200$. The tube is driven by a truncated periodic t^2 function with frequency f = 10 Hz, peak-to-peak stroke s

= 2.2 *mm*. The slug dimension is $D \times L = 3.556\ mm \times 10\ mm$, the same as in the experiment. The static, advancing, and receding contact angles are $65^0, 90^0,$ and 40^0 respectively. As the same model is used for both end caps, the polar graph for the rear end cap, coupled to the front end cap makes an approximately odd function about the static contact angle. The small loop inside each of the graphs is predicted, and it corresponds nicely to the experiments in figures 23 and 24.

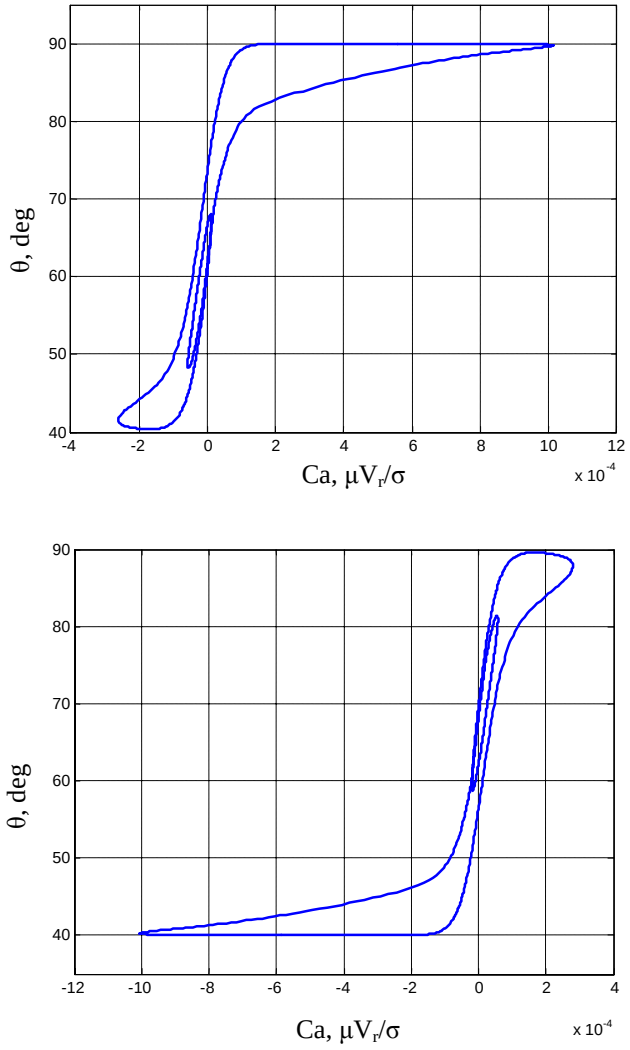

Figure 27. The polar graph is for the contact line on the forward side of the slug (upper graph). The contact line model $\theta_{rel} + 0.002\dot{\theta}_{rel} = \tanh(200V_r)$ is used as an edge condition for a 0-D simulation. As the same contact line model is used for both menisci, the polar graph for the contact line at the rear of the

moving slug (lower graph) is approximately axisymmetric to the front of the moving slug. Periodic t^2 forcing with f = 10 Hz, s = 2.2 *mm* is implemented.

The single slug net motion simulated with the 0-D approach is presented in figure 28 together with the experiments. The contact angle – contact line velocity relation used for simulation is that of figure 27, with $\theta_{adv} = 90^0$ and $\theta_{rec} = 40^0$. This is one of the simplest models considered in Section 3 for the harmonic forcing case. For simplicity, both contact lines for the forward and rear end caps of the slug are assumed to be governed by the same contact line model. As shown in figure 28, the simulated slug motion compares well with the experimental measurement (figure 21).

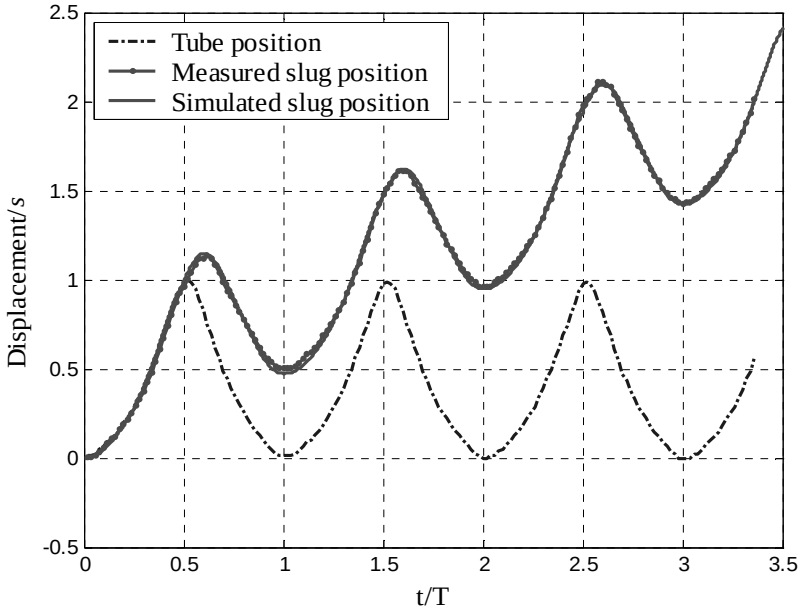

Figure 28. Simulated slug net motion compared with the experiment. The simulated pumping efficiency ≈ 47 %. The measurement is for the end cap on the front of the moving slug. This is the 'steady' net motion. Since the electrodynamic shaker is not stable initially, transient motion occurs prior to these data, and is therefore not presented. The tube motion is a 10-term t^2 function with frequency f = 10 Hz, stroke s = 2.2 *mm*. The slug is L = 10 *mm*, D = 3.556 *mm*.

The simulated contact angle variation and relative contact line velocity are presented in figure 29. They qualitatively agree with the measurement for the front cap shown in figure 22.

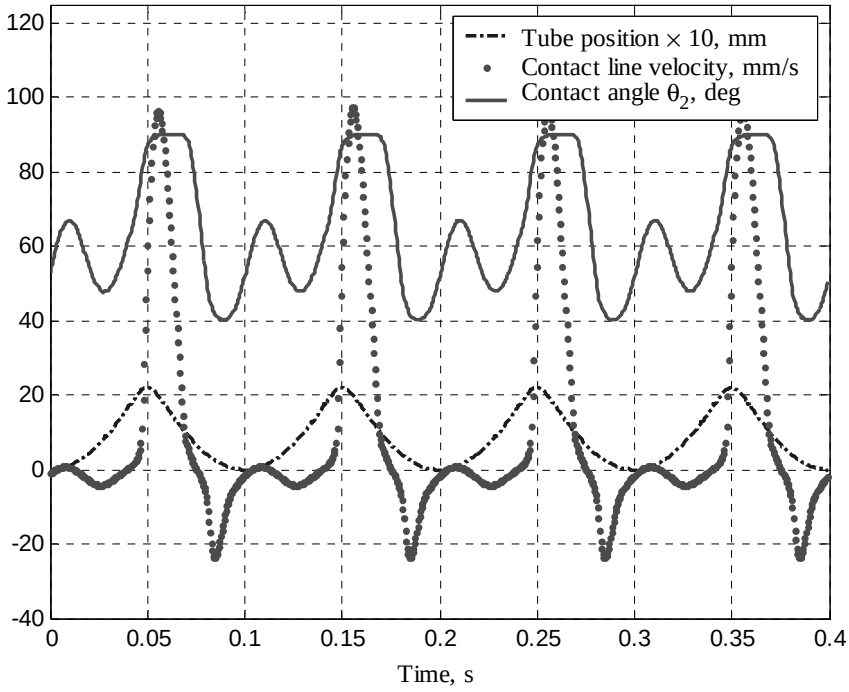

Figure 29. Contact angle, contact line velocity by a 0-D simulation corresponding to the experimental data shown in figure 22 (not in phase). The predicted motions are *almost* the same for the front and rear end caps as the same model is used for both in simulation.

The contact line motions predicted with the 0-D approach using contact line model (1) depend on the parameters in this edge condition. Although the contact angle hysteresis $\theta_{adv} - \theta_{rec}$ obviously affects the contact angle and contact line motion, the unsteady effects incorporated into the model are also important for pumping efficiency. In figure 30, the two contact line models have the same backbones but different coefficients for $\dot{\theta}_{rel}$. For the same tube motion, the larger oscillatory effect of $0.003\dot{\theta}_{rel}$ in (b) produces a larger pumping efficiency, 0.436, than that of the smaller oscillatory effect $0.001\dot{\theta}_{rel}$ in (a), 0.373. Apparently, more quantitative measurements for well controlled materials and tolerances are required to fit accurately these coefficients.

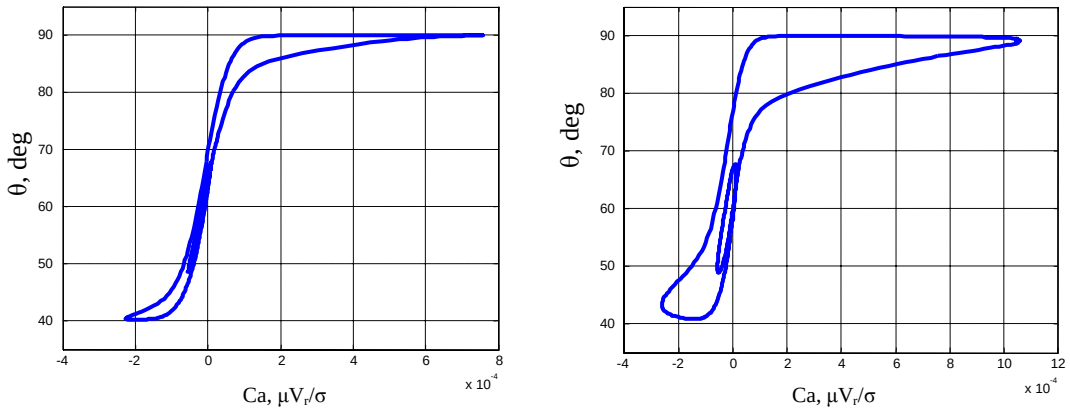

(a) pumping efficiency = 0.373 (b) pumping efficiency = 0.436

Figure 30. Predicted pumping efficiency is affected by the contact line model parameters. Pumping efficiency predicted is 0.373 in (a) for model $\theta_{rel} + 0.001\dot{\theta}_{rel} = \tanh 200V_r$ with less oscillatory effect; and 0.436 in (b) for model $\theta_{rel} + 0.003\dot{\theta}_{rel} = \tanh 200V_r$ with more oscillatory effect. The tube motion is a 10-term t^2 function with frequency f = 10 Hz, stroke s = 2 *mm*. The slug is L = 10 *mm*, D = 3.556 *mm*.

To determine optimal pumping for a given slug, the pumping efficiency is simulated for the same slug of size $D \times L = 3.556\,mm \times 10\,mm$ driven by the 10-term periodic t^2 function with different frequencies and strokes. The contact line model chosen for this simulation is $\theta_{rel} + 0.002\dot{\theta}_{rel} = 3V_r + \tanh 200V_r + 0.01V_r$ that gives a typical polar graph shown in figure 31 for asymmetric forcing, close to the measurement presented in figure 23. The maximum pumping efficiency contour plot simulated with the 0-D approach is presented in figure 32 and corresponds to the experiments in figure 26. The maximum pumping efficiency from this simulation is a function of the tube motion frequency and stroke as in the experiment. The figure shows the maximum pumping efficiency is in a region where the dimensionless frequency is 0.25 ~ 0.4 and the dimensionless stroke is 0.5 ~ 1. Compared with the experiments, the simulated optimal pumping coefficients decrease slower for larger tube motions, *i.e.*, higher frequencies or larger amplitudes. The simulated region of optimal pumping efficiency is close to that of

the experiments in figure 26 with slightly larger area extending to the lower right corner of the contour plot. However, the simulated maximum pumping efficiency is larger (~0.77) than the observations (~0.69).

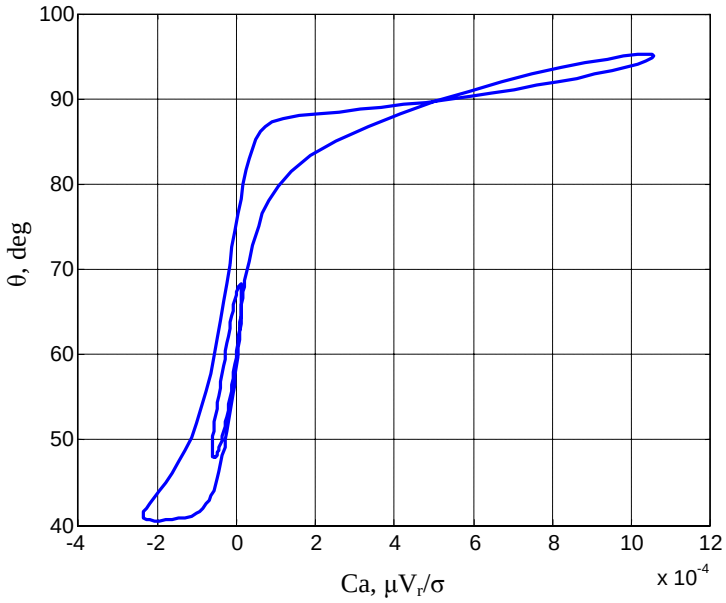

Figure 31. A typical polar graph corresponding to experiments presented in figure 23 is simulated for asymmetric forcing with contact line model $\theta_{rel} + 0.002\dot{\theta}_{rel} = 3V_r + \tanh 200V_r + 0.01Vr$.

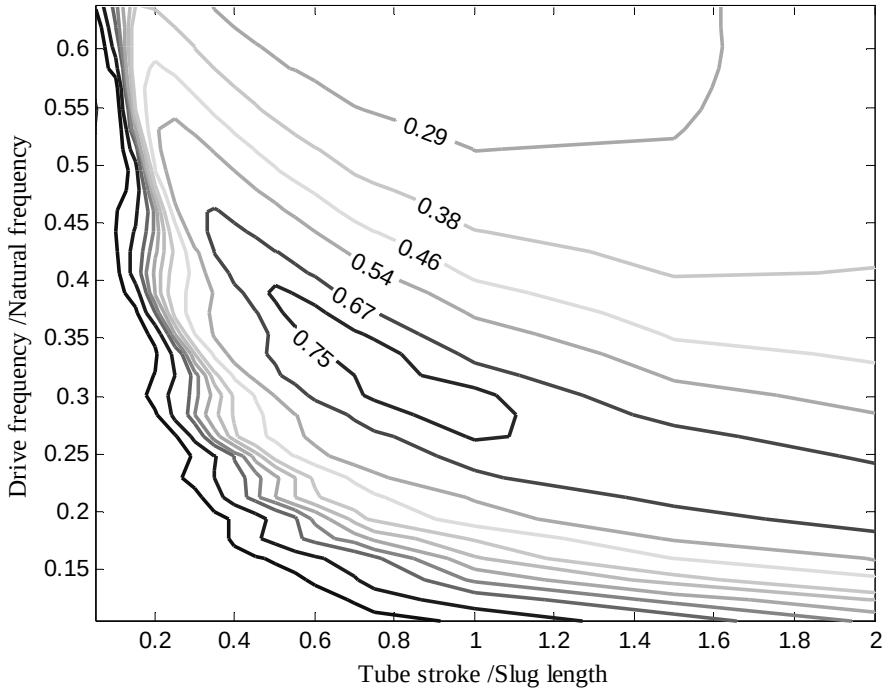

Figure 32. Simulated pumping efficiency presented for different drive frequency – stroke combinations. The corresponding experiment is presented in figure 26. The slug is of dimension $D \times L = 3.556\ mm \times 10\ mm$. The tube is driven by periodic t^2 motion represented by a filtered 10-term Fourier expansion. The lowest natural slosh frequency of the slug when $\theta_s = 65^0$ is 28.3 Hz according to the 2-D potential flow calculation for pinned contact lines (Bian *et al.* 2003).

There are several possible reasons for the over prediction by the 0-D approach. The most likely is that at large tube acceleration or velocity, the 0-D model prediction is inaccurate due to the no-longer-valid spherical end-cap assumption. Another possibility is that the difference in advancing and receding end caps observed in our experiments is not considered in our model. Also for a highly unsteady moving tube, a complicated flow pattern within the short slug may impose a much different drag than that of a steady pipe flow as approximated for the 0-D simulation.

5. Conclusions and discussion

The dynamic contact line of an immiscible liquid slug undergoing oscillatory motion in a circular tube has been studied. In the experiments due to the oscillatory flow, the surface condition of the tube wall is different than that of a dry tube. Focus is on the cases where no measurable thickness of film (maximum of 100 *nm*) is left by the moving meniscus. Oscillatory contact line motion is a complex process due to the unsteady motion and constant coating process in the vicinity of the contact line. The contact line relations depend on the oscillation frequencies and strokes. The unsteady effect is more sensitive to frequency, presumably due to inertia which is related directly to the acceleration term. The frequency also affects the surface wetting conditions near the contact line by an intermittent coating process. In Cocciaro *et al*. (1993) and Ting & Perlin's (1995) experiments with contact lines oscillating on a vertical plate, however, the contact line stroke had significant effect on the characteristics of the contact line relation.

To describe our experimental observations, an oscillatory contact line model is proposed where the unsteady effect is superposed on a unidirectional slow moving contact line model. Therefore with very slow oscillations, the contact angle–contact line velocity relation approaches the unidirectional contact line model (Dussan 1979). When oscillations are sufficiently large to coat the solid with thicker Newtonian films (O(1) μm), a contact angle–contact line velocity relationship similar to the experimental results of Ting & Perlin (1995) was observed. The experiments indicate that an ellipse-shaped oscillatory contact line model similar to Miles' (1990) can be used for sinusoidal motions exhibiting minimal contact line stick.

For small capillary number, Weber number and Bond number, a 0-D approach assuming spherical menisci is used to simulate the motion with the developed contact line model. The parameters of the model can be adjusted easily to fit the observations. With an even simpler reduced model, the simulated contact angle and contact line velocities are in qualitative agreement with the measurements. The 0-D approach also simulates the net slug displacement when the tube motion is asymmetric directionally (*e.g.* periodic t^2 function). The simulated slug motion agrees well with the experiments for slower motions where the spherical end cap assumption is presumably valid. The simulation also indicated that the oscillatory contact line model developed here is readily applicable to non-harmonic forcing.

Water is chosen as the substance for the liquid slug due to its large surface tension and relatively smaller viscosity. However, the consequent rapid contamination rate is an unfortunate drawback. It would be interesting to see the contact line relation for systems with different wetting properties. In our experimental study, the difference between apparent contact angles and macroscopic ones are neglected, and the gravity effects are approximated. Further measurement may be required to eliminate these problems, or identify these effects more quantitatively.

Finally, with the universal contact line model as the edge condition and a specific slip model in the vicinity of the contact line, a higher dimensional analysis should be readily accessible.

This research was supported by the NASA Microgravity Fluid Physics Program.

Appendix. Contradiction of time-harmonic wave motion assumption

We consider a standing capillary gravity wave at a solid vertical wall with Hocking's edge condition $\eta_x = c\,\eta_t$, the simplest contact line relationship relating contact line velocity to contact angle. For the sake of this argument, we assume the contact-line velocity is simple harmonic in time. At a small horizontal distance Δx from the wall, the surface elevation, $\eta(\Delta x, t) = \eta(0, t) + \eta_x \Delta x + o(\Delta x)$. The free surface at Δx is in phase with the surface elevation at the wall when $\eta(0, t)$ is at the crest or trough since the surface slope is zero. However, it is not in phase a quarter period later since the two locations do not cross the mean wave height at the same time. Therefore, there is a phase difference between the surface elevations $\eta(\Delta x, t)$ and $\eta(0, t)$ and both cannot both be simple harmonic in time. Extending this to more complicated relationships between contact angle versus contact-line velocity leads to a similar conclusion. A similar argument shows that the relation $\eta_x = \gamma\eta$ is compatible with time harmonicity.

REFERENCES

Agarwal, M., Bian, X., Perlin, M., & Schultz, W. W. 2001 The Motion of Water Slugs In Horizontally Oscillated Glass Tubes, APS 2001 meeting.

Benjamin, T. B. & Scott, J. C. 1979 Gravity-capillary waves with edge constraints. *J. Fluid Mech*. **92**, 241-267.

Bhatt, D., Newman, J. & Radke, C. J. 2002 Molecular simulation of disjoining-pressure isotherms for free liquid, Lennard-Jones thin films. *J. Phys. Chem*. B.**106**, 6529-6537.

Bian, X., Perlin, M., Schultz, W. W., & Agarwal, M. 2003 Axisymmetric slosh frequencies of a liquid mass in a circular cylinder. *Phys. Fluids*. **15**(12). 3659-3664.

Bretherton, F. P. 1961 The motion of long bubbles in tubes. *J. Fluid Mech*. **10**, 166-188.

Chang, H. C. 1994 Wave evolution on a falling film. *Ann. Rev. Fluid Mech.* **26**, 103-136.

Cocciaro, B., Faetti, S. & Festa, S. 1993 Experimental investigation of capillary effects on surface gravity waves: Non-wetting boundary conditions. *J. Fluid Mech*. **246**, 43-66.

Cox, R. G. 1986 The dynamics of the spreading of liquids on a solid surface. Part 1. Viscous flow. *J. Fluid Mech.* **168**, 169-194.

Cox, R. G. 1998 Inertial and viscous effects on dynamic contact angles. *J. Fluid Mech*. **357**, 249-278.

Decker, E. L., Frank, B., Suo, Y. & Garoff, S. 1999 Physics of contact angle measurement. *Colloids and Surface A*: **156**, 177-189.

Derjaguin, B. V., Churaev, N. V. & Muller, V. M. 1987 *Surface forces*, Consultants bureau, New York and London.

Dussan V., E. B. 1976 The moving contact line: The slip boundary condition. *J. Fluid Mech.* **77**, 665-684.

Dussan V., E. B. 1979 On the spreading of liquids on solid surfaces: Static and dynamic contact angles. *Annu. Rev. Fluid Mech.* **11**, 371- 400.

Dussan V., E. B., Ramé, E. & Garoff, S. 1991 On identifying the appropriate boundary conditions at a moving contact line: an experimental investigation. *J. Fluid Mech.* **230**, 97-116.

Giavedoni M. D., & Saita, F. A. 1997 The axisymmetric and plane cases of a gas phase steadily displacing a Newtonian liquid – A simultaneous solution of the governing equations. *Phys. Fluids* **9**, 2420- 2428.

Graham, D. R. & Higdon J. J. L. 2000 Oscillatory flow of droplets in capillary tubes. Part 1. Straight tubes, *J. Fluid Mech.* **425**, 31-53.

Graham-Eagle, J. 1983 A new method for calculating eigenvalues with applications to gravity-capillary waves with edge constraints, *Math. Proc. Camb. Phil. Soc.* **94**, 553.

Hocking, L. M. & Rivers, A. D. 1982 The spreading of a drop by capillary action. *J. Fluid Mech.* **121**, 425-442.

Huh, C. & Mason, S. G. 1977 The steady movement of a liquid meniscus in a capillary tube. *J. Fluid Mech*. **81**, 401-419.

Jiang, L., Perlin, M. & Schultz, W. W. 2004 Contact-line dynamics and damping for oscillatory free surface flows. *Phys. Fluids.* **16**, 748-758.

Kalinitchenko, V. A. & Sekerj_Zenkovitch, S. Ya. 1998 On the immiscible fluid displacement in capillary under oscillating pressure drop. *Experimental Thermal and Fluid Science.* **18**, 244-250.

Koplik J., Banavar J. R. & Willemsen J. F. 1989 Molecular dynamics of fluid flow at solid surfaces. *Phys. Fluids* A **1**, 781-794.

Koplik J. & Banavar J. R. 1995 Corner flow in the sliding plate problem. *Phys. Fluids.* **7**, 3118-3125.

Lowndes, J. 1980 The numerical simulation of the steady movement of a liquid meniscus in a capillary tube. *J. Fluid Mech*. **101**, 631-646.

Martinez, M. J. & Udell, K. S. 1989 Boundary integral analysis of the creeping flow of long bubbles in capillaries. *J. Appl. Mech*. **56**, 211.

Mitlin, V. S. & Petviashvili, N. V. 1994 Nonlinear dynamics of dewetting: kinetically stable structures. *Phys. Lett.* A. **192**, 323-326.

Ngan C. G. & Dussan V., E. B. 1989 On the nature of the dynamics contact angle: an experimental study. *J. Fluid Mech*. **209**, 191-226.

Ramé, E. & Garoff, S. 1996 Microscopic and macroscopic dynamic interface shapes and the interpretation of dynamic contact angles. *J. Colloid Interface Sci*. **177**, 234-244.

Sheng, P. & Zhou, M. 1992 Immiscible-fluid displacement: Contact-line dynamics and the velocity-dependent capillary pressure. *Phys. Rev*. A **45**, 5694-5708.

Miles, J. W. 1990 Capillary – viscous forcing of surface waves. *J. Fluid Mech*. **219**, 635-646.

Olbricht**,** K**.** L. 1996 Pore-scale prototypes of multiphase flow in porous media. *Annu. Rev. Fluid. Mech.* **28**, 187-213.

Perlin, M., Schultz, W. W., & Liu, Z. 2004 High Reynolds number oscillatory contact lines. *Wave Motion.* **40**, 41-56.

Ruschak, K. J. 1980 A method for incorporating free boundaries with surface tension in finite element fluid-flow simulators, *Int. J. Numer. Methods Eng.* **15**, 639-648.

Schwartz, L. W. & Eley, R. R. 1998 Simulation of droplet motion on low-energy and heterogeneous surfaces. *J. Colloid Interface Sci*. **202**, 173-188.

Somalinga, S. & Bose, A. 2000 Numerical investigation of boundary conditions for moving contact line problems. *Phys. Fluids* **12**, 499-510.

Stoev, K., Ramé, E. & Garoff, S, 1999 Effects of inertia on the hydrodynamics near moving contact lines. *Phys. Fluids* **11**, 3209-3216.

Taylor, G. I. 1961 Deposition of a viscous fluid on the wall of a tube. *J. Fluid Mech.* **10**, 161-165.

Thompson, P. A. & Robbins, M. O. 1989 Simulations of contact-line motion: slip and the dynamic contact angle. *Physical Review Letters* **63**, 766-769.

Tilley, B. S., Davis, S. H. & Bankoff, S. G. 2001 Unsteady Stokes flow near an oscillating, heated contact line. *J. Fluid Mech.* **438,** 339-362.

Ting, C. L. & Perlin, M. 1995 Boundary conditions in the vicinity of the contact line at a vertically oscillating upright plate: An experimental investigation. *J. Fluid Mech.* **395**, 263-300.

West, G. D. 1911 On the resistance to the motion of a thread of mercury in a glass tube. *Proc. Roy. Soc. Lond*. **86**, 20-25.

Wölk, G., Dreyer, M., & Rath, H. J. 1997 Damped oscillations of a liquid/gas surface upon step reduction in gravity. *J. Spacecraft and Rockets*, **34**, 110-117.

Young, G. W. and Davis, S. H. 1987 A plate oscillating across a liquid interface: effect of contact angle hysteresis. *J. Fluid Mech*. **174**, 327-356.